Stochastic static analysis of functionally graded sandwich nanoplates based on a novel stochastic meshfree computational framework

Baikuang Chen[a], Zhanjun Shao[b], A. S. Ademiloye[c], Delei Yang[d], Xuebing Zhang[a,*], Ping Xiang[b,e]

[a]*College of Civil Engineering, Xiangtan University, Xiangtan 411105, China;*
[b]*School of Civil Engineering, Central South University, Changsha 410075, China;*
[c]*Zienkiewicz Institute for Modelling, Data and AI, Faculty of Science and Engineering, Swansea University, Swansea, United Kingdom;*
[d]*College of Building Engineering, Huanghuai University, Henan Province 463000, China;*
[e]*National Engineering Research Center of High-speed Railway Construction Technology, Changsha 410018, China;*
*(*corresponding author's emails: zhangxb2002437@163.com)*

Abstract

In this study, the spatial variability of materials is incorporated into the static analysis of functionally graded sandwich nanoplates to achieve higher accuracy. Utilising a modified point estimation method and the radial point interpolation method, we develop a novel stochastic meshfree computational framework to deal with the material uncertainty. Higher-order shear deformation theory is employed to establish the displacement field of the plates. The elastic modulus of ceramic and metal (E_{c} and E_{m}) are treated as separate random fields and discretized through the Karhunen-Loève expansion (KLE) method. To improve the performance of procedure, the Wavelet-Galerkin method is introduced to solve the second type of Fredholm integral equation. Subsequently, substituting the random variables obtained by KLE into the stochastic computational framework, a high accuracy stochastic response of structures can be acquired. By comparing computed findings with those of Monte Carlo simulation, the accuracy and efficiency of developed framework are verified. Moreover, the results indicate that the plate's deflection exhibits varying sensitivities to the random fields E_{c} and E_{m}. Also, the sandwich configuration as well as power-law exponents affect the stochastic response of structures. These findings offer valuable insights for the optimized design of functionally graded sandwich nanoplates.

Keywords: Functionally graded sandwich nanoplate; Radial point interpolation method; Random field; Karhunen-Loève expansion method; Modified point estimation method.

1. Introduction

Functionally graded nanomaterials (FGMs) are a new type of non-homogeneous composites where the composition and microstructure continuously vary along the thickness, and this material gradation is customizable to fulfil specific application requirements [1,2]. As a result, FGMs offer numerous unique and exceptional properties, rendering them applicable across a diverse range of engineering fields, such as medical, civil, mechanical, aerospace engineering and defence industries [3,4].

Numerous studies on functionally graded (FG) nanostructures have been carried out and yielded a series of important results. Thai et al. [5,6] combined the modified coupled stress theory and higher-order shear deformation theory to examine the static, vibration and buckling behaviours of FG sandwiched nanoplates using the moving Kringing meshfree method. Vu et al. [7–9] analysed the mechanical behaviours of FG porous plates on elastic foundations based on a quasi-3D hyperbolic shear deformation theory. Their further contributions include the development of new logarithmic and arctangent exponential shear deformation theories [10,11]. Recently, Phung-Van et al. investigated the scale-dependent behaviour of functionally graded triply periodic minimal surface nanoplates [12] and honeycomb sandwich nanoplates [13]. This research applied nonlocal strain gradient theory to provide new findings on the microscopic complex mechanical behaviour of novel composite nanomaterials. Additionally, they investigate the nonlinear behaviours of FG nanoplates [14–16]. Hung et al. examined the free vibration of FG porous magneto-electro-elastic plates and honeycomb sandwich microplates using the isogeometric analysis method [17,18].

However, the majority of these vibration, static and buckling analysis of FG nanostructures are based on deterministic assumptions. In fact, most of structural material parameters are normally suboptimal as affected by construction, fabrication, ageing and the surrounding environment [19]. Therefore, it is necessary and reasonable to develop stochastic analysis methods for FGMs structures to optimise their design. Random field aims to characterize the spatial variability of random material or structural geometric parameters [20]. In the past decades, stochastic discretization techniques have been developed importantly as a necessary tool for stochastic field modelling. As an illustration, notable methods include the spatial averaging method [21], the centroid method [22], the spectral representation method [23], the wavelet expansion method [24] and the Karhunen-Loève expansion (KLE) method [25]. Particularly, KLE uses a set of random variables and deterministic eigenfunctions with eigenvalues to represent a stochastic process, which dramatically reduces the number of random variables required. Subsequently, Phoon et al. [26] and Tong et al. [27] improved the KLE to greatly enhance its applicability.

The discussion of random field modelling contributed to the development of various stochastic analysis theories, mainly including analytical methods and simulation methods. Monte Carlo simulation [28] is the most widely used simulation method, which requires a large number of simulated samples to compute the statistical moments, leading to inefficiency and expensive computational costs. Analytical methods include the Taylor expansion [29] or perturbation methods [30,31], the Neumann expansion method [32], the decomposition method [33], the polynomial chaos expansion method [34] and others. Taylor expansion or perturbation methods involve first-, second- or higher- order Taylor series expansion of output in terms of input random parameters, which usually entails costly computation of higher-order partial derivatives [35]. Neumann expansion method consists of Neumann series expansion of the inverse of random matrices, which is absolutely convergent. Nevertheless, the algebra and numerical effort required for a relatively low-order Neumann expansion can be enormous when there are a large number of random variables [36]. Decomposition method and polynomial chaos expansion method involve alternative series expansions. In this case, the decomposition method results in a series of terms that may not converge due to the recursive relationship of the expansion terms [37], while the polynomial chaos expansion approximates a square-integrable random variable by means of chaos polynomials. When a large number of input variables are involved, the polynomial coefficients grow exponentially, resulting in a huge computation [38]. In summary, all existing methods described above become computationally inefficient or less accurate when the number of input random variables is large. The point estimation method relies on Gaussian integration and does not involve solving for functional derivatives in reliability analysis [39]. By introducing multivariate function decomposition method [40] into the point estimation method, the multidimensional random variable function is approximated as the sum of multiple unidimensional random variable functions. Sample estimation points are then selected to calculate the statistical moments of stochastic responses using the Gaussian-Hermite integration principle. The modified point estimation method, called MPEM, is derivative-free and allows handling arbitrarily large numbers of random variables [41]. Notably, when the input uncertainties are high, the point estimation method yields inaccurate results as it approximates the second-moment properties of response using a finite number of probability concentrations [42]. Therefore, it is necessary to increase the number of sample estimation points to improve the accuracy of the computed results.

Unlike the finite element method, the meshfree method employs a node-based discretization approach to avoid the burdensome meshing or remeshing required. The element-free Galerkin method [43], the reproducing kernel particle method [44], the moving Kringing meshfree method [45] and the radial point interpolation method (RPIM) [46] are some of the meshfree methods available in the literature. Among these, RPIM is convenient due to the simplicity of its shape functions, which are formed based on radial and polynomial bases and possess Kronecker delta function properties [47,48]. In particular, a novel Tchebychev radial point interpolation method (TRPIM) was proposed by Kwak et al [49]. This method employs Tchebychev polynomial bases and radial bases to construct shape functions that approximate displacement components and applies them directly to the strong-form differential equations to obtain discretized control equations. Additionally, Thai et al. [50,51] developed a naturally stabilized nodal integration meshfree formulations for analysis of laminated composite and sandwich plates. These researches have significantly contributed to the application of meshfree methods in computational mechanics, providing an attractive alternative to the finite element method.

In this study, we developed a novel stochastic meshfree computational framework by incorporating the MPEM and RPIM. Compared with conventional stochastic analysis methods, the present method efficiently handles a large number of random variables and computes statistical moments using Gaussian integration without solving functional derivatives. Particularly, the advantages of RPIM meshfree method further enhances the framework's ability to analyse the stochastic response of complex structures. A three-layer functionally graded sandwich nanoplates (FGSNPs) with ceramic-metal combination is considered in this paper to investigate the effect of uncertainties in material parameters on its static response. Specifically, the elastic modulus of ceramic and metal are treated as separate random fields and discretized through the KLE method. The Wavelet-Galerkin method is introduced to solve the second type of Fredholm integral equation. Following that, the obtained stochastic variables are substituted into the MPEM-RPIM framework to compute deflections and stresses, enabling the evaluation of various stochastic responses of the structure. The results indicated that different types of FGSNPs exhibit varying sensitivities to uncertain material parameters in ceramics and metals. In particular, changes in the sandwich configuration and power-law exponents significantly affect the stochastic response of structures. Numerical examples confirmed the correctness and efficiency of the developed stochastic computational framework, providing valuable references for the optimized design of ceramic-metal functionally graded sandwich nanoplates.

2. Functionally graded sandwich plate

Consider rectangular FGSNPs with thickness h, length a and width b, as shown in Fig. 1. Fig. 1(a) shows a FGSNP of type A "FGSNP-A" with a ceramic core layer, and Fig. 1(b) is a FGSNP of type B "FGSNP-B" with a metal core layer. The edges of the plates are parallel to the x-axes and y-axes, and the vertical coordinates of its bottom, two interfaces, and top are denoted by h_0, h_1, h_2, h_3, respectively. FGSNPs consists of three isotropic elastic layers whose material properties of the top and bottom surface layers vary smoothly only in the thickness direction. In this paper, all numerical examples are described using simple symbols, for instance, the symbol 1-2-1 indicates that the core thickness is twice as thick as the top/bottom, while the top and bottom panels have the same thickness.

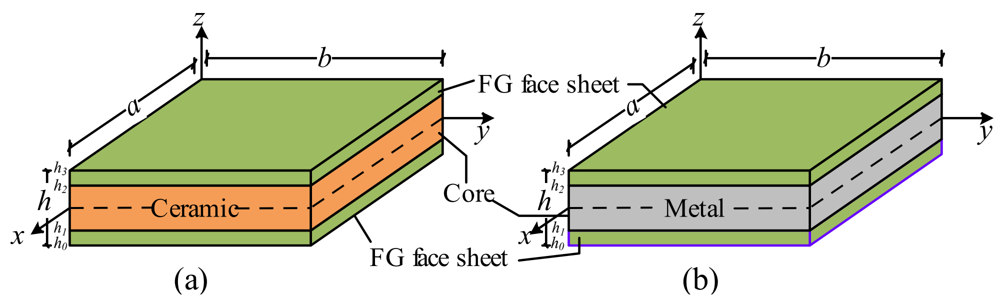

Fig. 1 The geometric configuration of FGSNPs: (a) FGSNP-A; (b) FGSNP-B.

For the FGSNP-A with a power-law distribution, the volume fraction of ceramic in the k-th layer is expressed as follows [5],

$$V^{(1)}(z)=\left(\frac{z-h_0}{h_1-h_0}\right)^p,\quad h_0\le z\le h_1;$$
$$V^{(2)}(z)=1,\quad h_1\le z\le h_2;$$
$$V^{(3)}(z)=\left(\frac{z-h_3}{h_2-h_3}\right)^p,\quad h_2\le z\le h_3. \tag{1}$$

For the FGSNP-B with a power-law distribution, the volume fraction of ceramic in the k-th layer is expressed as follows [52],

$$V^{(1)}(z)=1-\left(\frac{z-h_0}{h_1-h_0}\right)^p,\quad h_0\le z\le h_1;$$
$$V^{(2)}(z)=0,\quad h_1\le z\le h_2;$$
$$V^{(3)}(z)=1-\left(\frac{z-h_3}{h_2-h_3}\right)^p,\quad h_2\le z\le h_3. \tag{2}$$

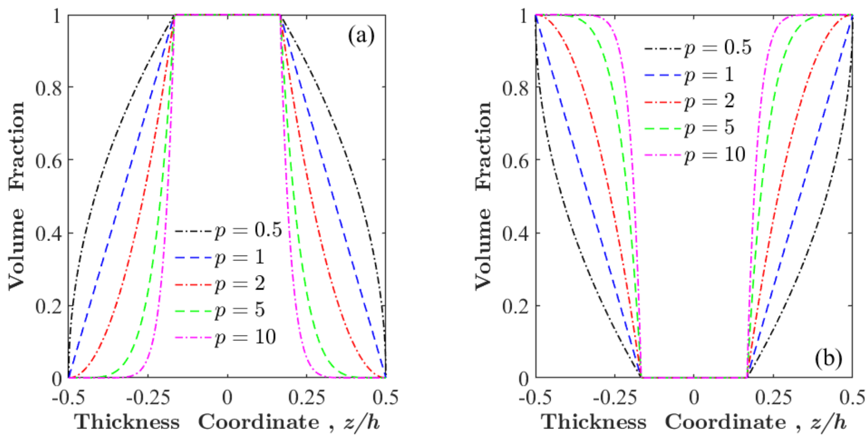

Fig. 2 The variation of the volume fraction for ceramics along the thickness of FGSNPs with different power-law exponent p: (a) FGSNP-A; (b) FGSNP-B

The variation of ceramic volume fraction of FGSNPs along the thickness are illustrated in Fig. 2. According to a mixing rule [53], the effective material properties of the k-th layer can be calculated as,

$$P^{(k)}(z)=P_{\mathrm{m}}+\left(P_{\mathrm{c}}-P_{\mathrm{m}}\right)V^{(k)}(z) \tag{3}$$

where P represents the effective material properties such as elastic modulus E, density ρ and Poisson's ratio ν; $V^{(k)}(z)$ denotes the volume fraction of ceramics along the plate thickness; and the subscripts ‘m’ and ‘c’ denote the metal and ceramic compositions, respectively.

3. Formula derivation

3.1 Displacement of HSDT

The high-order shear deformation theory has been widely applied to the computation of plate and shell structures in current study [54]. According to HSDT, the displacement component at any point on the k-th layer of a sandwich plate can be expressed as,

$$\begin{aligned} u^{(k)}(x,y,z) &= u_0(x,y) - z\beta_x + f(z)\phi_x(x,y), \\ v^{(k)}(x,y,z) &= v_0(x,y) - z\beta_y + f(z)\phi_y(x,y), \\ w^{(k)}(x,y,z) &= w_0(x,y) \end{aligned} \tag{4}$$

where u^k and v^k are the in-plane displacements at any point (x,y,z) of the k-th layer; u_0, v_0 and w_0 are the displacement components of the mid-plane along the x,y,z directions; ϕ_x and ϕ_y are the rotational inertia of the mid-plane about y-axis and x-axis, respectively; $\beta_x = w_{0,x}$ as well as $\beta_y = w_{0,y}$.

To satisfy the zero shears at the inferior and superior surfaces, Eq. (4) introduces a shape function $f(z)$ varying along the thickness of FGSNPs. In this study, $f(z) = z - 4z^2/(3h^2)$ proposed by Reddy [55] is adopted.

The displacement of Eq. (4) can be written in compact form as follows,

$$\boldsymbol{u}^k = \boldsymbol{u}_0 + z\boldsymbol{u}_1 + f(z)\boldsymbol{u}_2 \tag{5}$$

with,

$$\boldsymbol{u}_0 = \begin{Bmatrix} u_0 \\ v_0 \\ w_0 \end{Bmatrix};\ \boldsymbol{u}_1 = \begin{Bmatrix} -\beta_x \\ -\beta_y \\ 0 \end{Bmatrix};\ \boldsymbol{u}_2 \begin{Bmatrix} \phi_x \\ \phi_y \\ 0 \end{Bmatrix} \tag{6}$$

The displacement-strain relations for layer k can be written as,

$$\begin{aligned} \boldsymbol{\varepsilon} &= \begin{Bmatrix} \varepsilon_{xx} & \varepsilon_{yy} & \tau_{xy} \end{Bmatrix}^{\mathrm{T}} = \boldsymbol{\varepsilon}_0 + z\boldsymbol{\varepsilon}_1 + f(z)\boldsymbol{\varepsilon}_2, \\ \boldsymbol{\tau} &= \begin{Bmatrix} \tau_{xz} & \tau_{yz} \end{Bmatrix}^{\mathrm{T}} = \boldsymbol{\varepsilon}_0^{\mathrm{s}} + f'(z)\boldsymbol{\varepsilon}_1^{\mathrm{s}} \end{aligned} \tag{7}$$

with,

$$\begin{aligned} &\boldsymbol{\varepsilon}_0 = \begin{Bmatrix} u_{0,x} \\ v_{0,x} \\ u_{0,y} + v_{0,x} \end{Bmatrix},\ \boldsymbol{\varepsilon}_1 = -\begin{Bmatrix} \beta_{x,x} \\ \beta_{y,x} \\ \beta_{x,y} + \beta_{y,x} \end{Bmatrix}, \\ &\boldsymbol{\varepsilon}_2 = \begin{Bmatrix} \phi_{x,x} \\ \phi_{y,y} \\ \phi_{x,y} + \phi_{y,x} \end{Bmatrix},\ \boldsymbol{\varepsilon}_0^{\mathrm{s}} = \begin{Bmatrix} w_{0,x} - \beta_x \\ w_{0,y} - \beta_y \end{Bmatrix},\ \boldsymbol{\varepsilon}_1^{\mathrm{s}} = \begin{Bmatrix} \phi_x \\ \phi_y \end{Bmatrix}. \end{aligned} \tag{8}$$

By neglecting $\sigma_z^{(k)} = \sigma_3^{(k)}$ for each orthogonal layer in the laminate structure, the constitutive equation for the k-th orthogonal layer of laminate can be expressed as,

$$\begin{Bmatrix} \sigma_{xx}^{(k)} \\ \sigma_{yy}^{(k)} \\ \tau_{xy}^{(k)} \\ \tau_{xz}^{(k)} \\ \tau_{yz}^{(k)} \end{Bmatrix} = \begin{bmatrix} Q_{11}^{(k)} & Q_{12}^{(k)} & 0 & 0 & 0 \\ Q_{21}^{(k)} & Q_{22}^{(k)} & 0 & 0 & 0 \\ 0 & 0 & Q_{66}^{(k)} & 0 & 0 \\ 0 & 0 & 0 & Q_{55}^{(k)} & 0 \\ 0 & 0 & 0 & 0 & Q_{44}^{(k)} \end{bmatrix} \begin{Bmatrix} \varepsilon_{xx}^{(k)} \\ \varepsilon_{yy}^{(k)} \\ \gamma_{xy}^{(k)} \\ \gamma_{xz}^{(k)} \\ \gamma_{yz}^{(k)} \end{Bmatrix} \tag{9}$$

where subscripts 1, 2 and 3 correspond to the x, y and z directions, respectively. The FGSNPs in this study consist of isotropic elastic layers, $Q_{ij}^{(k)}$ can be written as,

$$Q_{11}^{(k)} = Q_{22}^{(k)} = \frac{E^{(k)}(z)}{1-\nu^2},\ Q_{12}^{(k)} = Q_{21}^{(k)} = \frac{\nu E^{(k)}(z)}{1-\nu^2},$$
$$Q_{66}^{(k)} = Q_{55}^{(k)} = Q_{44}^{(k)} = \frac{E^{(k)}(z)}{2(1+\nu)} \tag{10}$$

3.2 Radial point interpolation method

Let us consider a support domain Ω_s that has a set of arbitrarily distributed nodes as shown in Fig 3. The approximate function $u^h(\boldsymbol{x})$ can be estimated for all values of nodes within the support domain based on radial point interpolation method (RPIM) by using radial basis function $R_i(\boldsymbol{x})$ and polynomial basis function $p_j(\boldsymbol{x})$ [56]. Nodal value of approximate function evaluated at the node $\boldsymbol{x}_i$ inside support domain is assumed to be u_i.

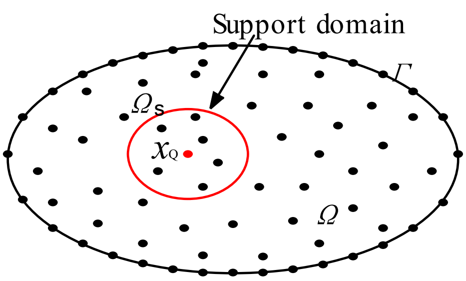

Fig 3 Supporting domain and supporting nodes of the meshless method.

$$u^{\mathrm{h}}(\boldsymbol{x}) = \sum_{i=1}^{n} R_i(\boldsymbol{x}) a_i + \sum_{j=1}^{m} p_j(\boldsymbol{x}) b_j = \boldsymbol{R}^{\mathrm{T}}(\boldsymbol{x})\boldsymbol{a} + \boldsymbol{p}^{\mathrm{T}}(\boldsymbol{x})\boldsymbol{b} \tag{11}$$

For a two-dimensional (2D) problem, the second-order polynomial basis functions are taken as,

$$\boldsymbol{p}(\boldsymbol{x}) = \begin{bmatrix} 1 & x & y & x^2 & xy & y^2 \end{bmatrix}^{\mathrm{T}} \tag{12}$$

thus, we have $m = 6$. And the radial basis functions $\boldsymbol{R}(\boldsymbol{x})$ is defined as,

$$\boldsymbol{R}(\boldsymbol{x}) = \left[R_1(x), R_2(x), \cdots, R_n(x) \right]^{\mathrm{T}} \tag{13}$$

where the number of terms n is the number of support nodes in supporting domain Ω_{s}.

There are various commonly used radial basis functions (RBF), in this paper Multi-quadratic (MQ) radial basis function is adopted and its expression is as follows,

$$R_i(x) = \left[r^2 + (\alpha h)^2 \right]^{\beta} \tag{14}$$

where r denotes the distance function, and for the 2D problem we have $r = \sqrt{(x - x_i)^2 + (y - y_i)^2}$; h is the average node spacing; α and β are the shape coefficients, and they are set to 1 and 1.03 respectively according to [57].

The following generic function is constructed from the set of dispersed nodes $\{x_i\}_{i=1}^{n} (\forall x_i \in \Omega_{\mathrm{s}})$ on the local support domain Ω_{s} at the computation point $\boldsymbol{x}$,

$$J_1 = \sum_{i=1}^{n} \left[\boldsymbol{R}^{\mathrm{T}}(\boldsymbol{x}_i)\boldsymbol{a} + \boldsymbol{p}^{\mathrm{T}}(\boldsymbol{x}_i)\boldsymbol{b} - \hat{u}_i \right] \tag{15}$$

$$J_2 = \sum_{i=1}^{n} p_j(x_i) b_i,\ j = 1, 2, \cdots, m \tag{16}$$

Let $J_1 = 0,\ J_2 = 0$, the equation (17) can be obtained as follows,

$$\begin{bmatrix} \boldsymbol{R}_n & \boldsymbol{P}_{\boldsymbol{m}} \\ \boldsymbol{P}_{\boldsymbol{m}}^{\mathrm{T}} & \boldsymbol{0} \end{bmatrix} \begin{bmatrix} \boldsymbol{a} \\ \boldsymbol{b} \end{bmatrix} = \begin{bmatrix} \hat{\boldsymbol{U}}_s \\ \boldsymbol{0} \end{bmatrix} \tag{17}$$

where $\widehat{\boldsymbol{U}}_s$ is the vector of all the support node displacements; $\boldsymbol{R}_n$ and $\boldsymbol{P}_m$ are express as:

$$\boldsymbol{R}_{\boldsymbol{n}} = \begin{bmatrix} R_1(x_1) & R_2(x_1) & \cdots & R_n(x_1) \\ R_1(x_2) & R_2(x_2) & \cdots & R_n(x_2) \\ \vdots & \vdots & \ddots & \vdots \\ R_1(x_n) & R_2(x_n) & \cdots & R_n(x_n) \end{bmatrix} \tag{18}$$

$$\boldsymbol{P}_{\boldsymbol{m}} = \begin{bmatrix} p_1(x_1) & p_2(x_1) & \cdots & p_m(x_1) \\ p_1(x_2) & p_2(x_2) & \cdots & p_m(x_2) \\ \vdots & \vdots & \ddots & \vdots \\ p_1(x_n) & p_2(x_n) & \cdots & p_m(x_n) \end{bmatrix} \tag{19}$$

Solving Eq. (17) yields,

$$\boldsymbol{a} = \left[\boldsymbol{R}_{\boldsymbol{n}}^{-1} - \boldsymbol{R}_{\boldsymbol{n}}^{-1} \boldsymbol{P}_{\boldsymbol{m}} \left(\boldsymbol{P}_{\boldsymbol{m}}^{\mathrm{T}} \boldsymbol{R}_{\boldsymbol{n}}^{-1} \boldsymbol{P}_{\boldsymbol{m}} \right)^{-1} \boldsymbol{P}_{\boldsymbol{m}}^{\mathrm{T}} \boldsymbol{R}_{\boldsymbol{n}}^{-1} \right] \hat{\boldsymbol{U}}_s = \boldsymbol{G}_a \hat{\boldsymbol{U}}_s \tag{20}$$

$$\boldsymbol{b} = \left(\boldsymbol{P}_{\boldsymbol{m}}^{\mathrm{T}} \boldsymbol{R}_{\boldsymbol{n}}^{-1} \boldsymbol{P}_{\boldsymbol{m}}\right)^{-1} \boldsymbol{P}_{\boldsymbol{m}}^{\mathrm{T}} \boldsymbol{R}_{\boldsymbol{n}}^{-1} \hat{\boldsymbol{U}}_s = \boldsymbol{G}_b \hat{\boldsymbol{U}}_s \tag{21}$$

thus, Eq. (11) can be rewritten as,

$$\begin{aligned} u^{\mathrm{h}}(\boldsymbol{x}) &= \boldsymbol{R}^{\mathrm{T}}(\boldsymbol{x})\boldsymbol{a} + \boldsymbol{p}^{\mathrm{T}}(\boldsymbol{x})\boldsymbol{b} = \left[\boldsymbol{R}^{\mathrm{T}}(\boldsymbol{x})\boldsymbol{G}_a + \boldsymbol{p}^{\mathrm{T}}(\boldsymbol{x})\boldsymbol{G}_b\right]\hat{\boldsymbol{U}}_s \\ &= \sum_{i=1}^{n} \varphi_i(x)\hat{u}_i = \boldsymbol{\Phi}(\boldsymbol{x})\hat{\boldsymbol{U}}_s \end{aligned} \tag{22}$$

in which the shape function is defined,

$$\boldsymbol{\Phi}(\boldsymbol{x}) = \boldsymbol{R}^{\mathrm{T}}(\boldsymbol{x})\boldsymbol{G}_a + \boldsymbol{p}^{\mathrm{T}}(\boldsymbol{x})\boldsymbol{G}_b \tag{23}$$

Another important issue that must be considered in meshfree methods is the selection of the radius of the support domain. As shown in Fig 3, for a computational node $\boldsymbol{x}_{\mathrm{Q}}$, the radius of its support domain d_m is determined by [5],

$$d_m = \alpha_c d_c \tag{24}$$

where d_c is a characteristic length related to the nodal spacing while α_c denotes the scale factor. The value of α_c will be determined in a subsequent numerical example.

3.3 Governing equation

For the static bending problem of FGSNPs, the application of the principle of virtual work leads to the following equation [52],

$$\delta U = \int_V \sigma_{ij}^{(k)} \delta\varepsilon_{ij}^{(k)} \mathrm{dV} - \int_\Omega q_0 \delta w \mathrm{d}\Omega \tag{25}$$

where q_0 is the uniform sinusoidal transverse load. Substituting Eqs. (7) - (10) into Eq. (25), and making $\delta U = 0$, the weak form of governing equation can be expressed as follows,

$$\int_\Omega \delta\bar{\boldsymbol{\varepsilon}}^{\mathrm{T}} \boldsymbol{Q}^{\mathrm{b}} \bar{\boldsymbol{\varepsilon}} \mathrm{d}\Omega + \int_\Omega \delta\bar{\boldsymbol{\gamma}}^{\mathrm{T}} \boldsymbol{Q}^{\mathrm{s}} \bar{\boldsymbol{\gamma}} \mathrm{d}\Omega = \int_\Omega \delta w q_0 \mathrm{d}\Omega \tag{26}$$

where,

$$\begin{gathered} \bar{\boldsymbol{\varepsilon}} = \begin{Bmatrix} \boldsymbol{\varepsilon}_0 \\ \boldsymbol{\varepsilon}_1 \\ \boldsymbol{\varepsilon}_2 \end{Bmatrix}, \; \bar{\boldsymbol{\gamma}} = \begin{Bmatrix} \boldsymbol{\varepsilon}_0^{\mathrm{s}} \\ \boldsymbol{\varepsilon}_1^{\mathrm{s}} \end{Bmatrix}, \; \boldsymbol{Q}^{\mathrm{b}} = \begin{bmatrix} \mathbf{A} & \mathbf{B} & \mathbf{E} \\ \mathbf{B} & \mathbf{D} & \mathbf{F} \\ \mathbf{E} & \mathbf{F} & \mathbf{H} \end{bmatrix}, \; \boldsymbol{Q}^{\mathrm{s}} = \begin{bmatrix} \mathbf{A}^{\mathrm{s}} & \mathbf{B}^{\mathrm{s}} \\ \mathbf{B}^{\mathrm{s}} & \mathbf{D}^{\mathrm{s}} \end{bmatrix}, \\ \left(A_{ij}, B_{ij}, D_{ij}, E_{ij}, F_{ij}, H_{ij}\right) = \int_{-h/2}^{h/2} \left(1, z.z^2, f(z), zf(z), f^2(z)\right) Q_{ij} \mathrm{d}z \quad \text{where } (i,\ j = 1,\ 2,\ 6), \\ (A_{ij}^{\mathrm{s}},\ B_{ij}^{\mathrm{s}},\ D_{ij}^{\mathrm{s}}) = \int_{-h/2}^{h/2} \left(1, f'(z), f'^2(z)\right) Q_{ij} \ \mathrm{d}z \ \text{ where } (i,\ j = 4,\ 5). \end{gathered} \tag{27}$$

According to RPIM shape function, the displacement field can be expressed as,

$$\boldsymbol{u}^{\mathrm{h}}(x,y)=\sum_{i=1}^{n}\begin{bmatrix}\varphi_i(x,y) & 0 & 0 & 0 & 0 & 0 & 0\\ 0 & \varphi_i(x,y) & 0 & 0 & 0 & 0 & 0\\ 0 & 0 & \varphi_i(x,y) & 0 & 0 & 0 & 0\\ 0 & 0 & 0 & \varphi_i(x,y) & 0 & 0 & 0\\ 0 & 0 & 0 & 0 & \varphi_i(x,y) & 0 & 0\\ 0 & 0 & 0 & 0 & 0 & \varphi_i(x,y) & 0\\ 0 & 0 & 0 & 0 & 0 & 0 & \varphi_i(x,y)\end{bmatrix}\begin{Bmatrix}u_{0i}\\ v_{0i}\\ w_{0i}\\ \beta_{xi}\\ \beta_{yi}\\ \phi_{xi}\\ \phi_{yi}\end{Bmatrix}$$

$$=\sum_{i=1}^{n}\boldsymbol{\Phi}_i(x,y)\boldsymbol{U}_i \tag{28}$$

where $\boldsymbol{U}_i$ is a displacement vector containing n support nodes.

Substituting Eq. (28) into Eq. (27), the bending and shear strains can be expressed as,

$$\bar{\boldsymbol{\varepsilon}}=\begin{Bmatrix}\boldsymbol{\varepsilon}_0\\ \boldsymbol{\varepsilon}_1\\ \boldsymbol{\varepsilon}_2\end{Bmatrix}=\sum_{i=1}^{n}\begin{Bmatrix}\boldsymbol{B}_i^0\\ \boldsymbol{B}_i^1\\ \boldsymbol{B}_i^2\end{Bmatrix}\boldsymbol{U}_i=\sum_{i-1}^{n}\bar{\boldsymbol{B}}_i^{\mathrm{b}}\boldsymbol{U}_i,\ \ \bar{\boldsymbol{\gamma}}=\begin{Bmatrix}\boldsymbol{\varepsilon}_0^{\mathrm{s}}\\ \boldsymbol{\varepsilon}_1^{\mathrm{s}}\end{Bmatrix}=\sum_{i-1}^{n}\begin{Bmatrix}\boldsymbol{B}_i^{\mathrm{s}0}\\ \boldsymbol{B}_i^{\mathrm{s}1}\end{Bmatrix}\boldsymbol{U}_i=\sum_{i=1}^{n}\bar{\boldsymbol{B}}_i^{\mathrm{s}}\boldsymbol{U}_i \tag{29}$$

where,

$$\boldsymbol{B}_i^0=\begin{bmatrix}\varphi_{i,x} & 0 & 0 & 0 & 0 & 0 & 0\\ 0 & \varphi_{i,y} & 0 & 0 & 0 & 0 & 0\\ \varphi_{i,y} & \varphi_{i,x} & 0 & 0 & 0 & 0 & 0\end{bmatrix},\ \ \boldsymbol{B}_i^{\mathrm{s}0}=\begin{bmatrix}0 & 0 & \varphi_{i,x} & -\varphi_i & 0 & 0 & 0\\ 0 & 0 & \varphi_{i,y} & 0 & -\varphi_i & 0 & 0\end{bmatrix},$$

$$\boldsymbol{B}_i^1=\begin{bmatrix}0 & 0 & 0 & -\varphi_{i,x} & 0 & 0 & 0\\ 0 & 0 & 0 & 0 & -\varphi_{i,y} & 0 & 0\\ 0 & 0 & 0 & -\varphi_{i,y} & -\varphi_{i,x} & 0 & 0\end{bmatrix},\ \ \boldsymbol{B}_i^{\mathrm{s}1}=\begin{bmatrix}0 & 0 & 0 & 0 & 0 & \varphi_i & 0\\ 0 & 0 & 0 & 0 & 0 & 0 & \varphi_i\end{bmatrix},$$

$$\boldsymbol{B}_i^2=\begin{bmatrix}0 & 0 & 0 & 0 & 0 & \varphi_{i,x} & 0\\ 0 & 0 & 0 & 0 & 0 & 0 & \varphi_{i,y}\\ 0 & 0 & 0 & 0 & 0 & \varphi_{i,y} & \varphi_{i,x}\end{bmatrix}. \tag{30}$$

Substituting Eqs. (30) and (29) into Eq. (26), the discrete form of governing equation for static bending of FGSNPs can be obtained as,

$$\boldsymbol{KU}=\boldsymbol{F} \tag{31}$$

where $\boldsymbol{U}$ is the global displacement vector; $\boldsymbol{K}$ and $\boldsymbol{F}$ denote the global stiffness matrix and force vector, respectively, which are computed as,

$$\boldsymbol{K} = \int_{\Omega} \left(\bar{\boldsymbol{B}}^{\mathrm{b}}\right)^{\mathrm{T}} \boldsymbol{Q}^{\mathrm{b}} \bar{\boldsymbol{B}}^{\mathrm{b}} \mathrm{d}\Omega + \int_{\Omega} \left(\bar{\boldsymbol{B}}^{\mathrm{s}}\right)^{\mathrm{T}} \boldsymbol{Q}^{\mathrm{s}} \bar{\boldsymbol{B}}^{\mathrm{s}} d\Omega \tag{32}$$

$$\boldsymbol{F} = \int_{\Omega} q_0 \begin{bmatrix} 0 & 0 & \varphi_i & 0 & 0 & 0 & 0 \end{bmatrix}^{\mathrm{T}} \mathrm{d}\Omega \tag{33}$$

To solve the numerical integration of Eqs. (32) and (33), the problem domain needs to be discretized into a set of background mesh. In this study, a square plate is divided into a rectangular background mesh with 21 × 21 nodes at the mesh vertices, as illustrated in Fig. 4(a). Then the integration for each background cell is performed using a set of 4 × 4 Gaussian points.

It is worth noting that structures with irregular polygons or simple curved edges will cause background mesh distortion and irregular nodal distributions as shown in Fig. 4(b), for which the irregular mesh can be transformed into a regular rectangle by coordinate mapping. However, for structures with complex irregular geometry, seen in Fig. 4(c), the Gaussian integral becomes highly complex and inapplicable. Thus, new methods are required to solve the integration for integration in domains with irregular nodal distributions. Effective solutions include the stabilized conforming nodal integration by Chen et al. [58] and the naturally stabilized nodal integration by Thai et al. [59,60].

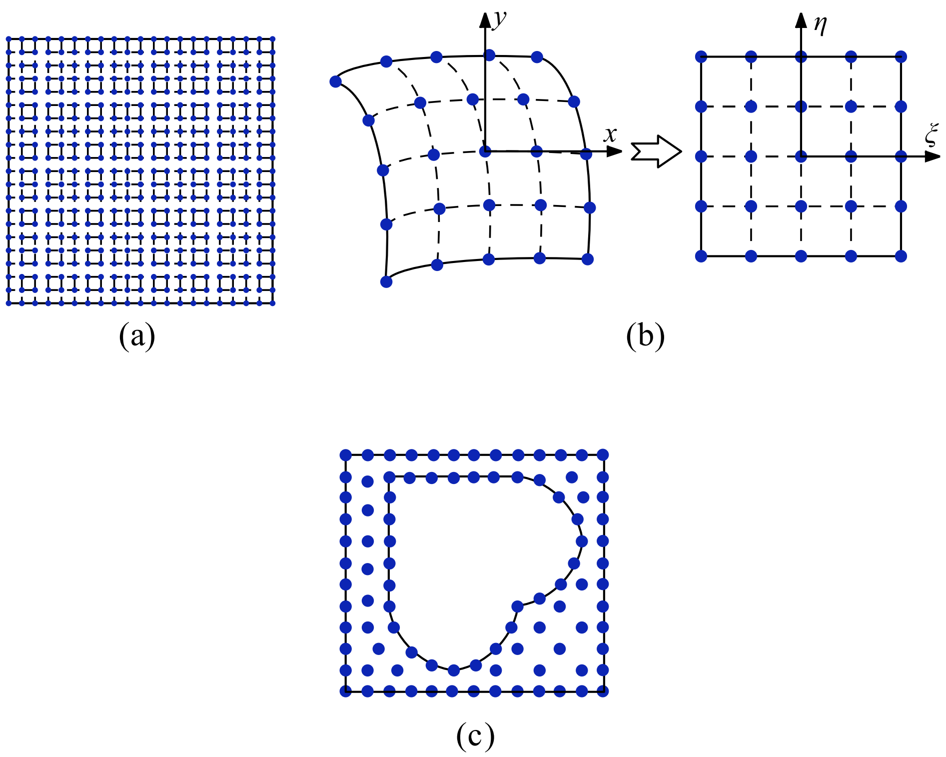

Fig 4. Geometry and nodes distribution: (a) rectangle; (b) simple curved shape; (c) complex irregular shape.

4. Approaches for stochastic analysis

4.1 Discretization of random fields

4.1.1 Karhunen–Loève expansion

A one-dimensional (1D) random field $X(x,\gamma)$ is a function of the spatial coordinates x and random variable θ. $\bar{X}(x,\gamma)$ is mean value of $X(x,\gamma)$, and $\hat{X}(x,\gamma)$ is a zero-mean random field, then the stochastic process can be formulated as,

$$X(x,\gamma) = \bar{X}(x,\gamma) + \hat{X}(x,\gamma) \tag{34}$$

The covariance function $C(x_1,x_2)$ of this random field is a positive definite function with bounded symmetry, which by Mercer's theorem [61], expands to,

$$C(x_1,x_2) = \sum_{i=1}^{\infty} \lambda_i f_i(x_1) f_i(x_2) \tag{35}$$

where λ_i and $f_i(x)$ are the eigenvalues and eigenfunctions of covariance function, which can be obtained by solving the Fredholm integral equation of the second kind as shown in Eq. (36),

$$\int_{\Omega} C(x_1,x_2) f_i(x_2)\mathrm{dx}_2 = \lambda_i f_i(x_1) \tag{36}$$

Symmetry and positive definiteness of covariance function will render the eigenfunctions to be orthogonal and complete and thus,

$$\int_{\Omega} f_i(x) f_j(x)\mathrm{dx} = \delta_{ij} \tag{37}$$

where Ω is a random field region and the common covariance functions are Exponential and Gaussian as follows [35],

$$\begin{cases} C(x_1,x_2) = \sigma^2 e^{-|x_1-x_2|/c} & \text{(Exponential type)} \\ C(x_1,x_2) = \sigma^2 e^{-(x_1-x_2)^2/c^2} & \text{(Gaussial type)} \end{cases} \tag{38}$$

where σ is standard deviation and c is correlative length.

With $f_i(x)$ as the basis function to expand $\hat{X}(x,\gamma)$, the stochastic process can be rewritten as,

$$X(x,\gamma) = \bar{X}(x,\gamma) + \sum_{i=1}^{\infty} \gamma_i \sqrt{\lambda_i} f_i(x) \tag{39}$$

is called the Karhunen-Loève expansion [25]. γ_i is a set of uncorrelated random variables. When $X(x,\gamma)$ belongs to a Gaussian random process, γ_i obeys a standard normal distribution. In practice, Eq. (39) is usually truncated after the N term as needed, so that the random field $X(x,\gamma)$ is represented by the KLE,

$$X(x,\gamma) = \bar{X}(x,\gamma) + \sum_{i=1}^{N} \gamma_i \sqrt{\lambda_i} f_i(x) \tag{40}$$

4.1.2 Wavelet-Galerkin method

For the exponential covariance function of a 1D random field, the analytical solution of Fredholm integral equations of the second kind is [19],

$$\begin{cases} \lambda_i = \dfrac{2c\sigma^2}{c^2\omega_i^2+1} \\ f_i(x) = \dfrac{1}{\sqrt{\left(c^2\omega_i^2+1\right)L/2+c}}[c\omega_i\cos(\omega_i x)+\sin(\omega_i x)] \end{cases} \tag{41}$$

where L is the length of a 1D random field and ω_i can be found from the following transcendental equation,

$$(c^2\omega_i^2-1)\sin(\omega_i L) = 2c\omega_i\cos(\omega_i L) \tag{42}$$

However, the analytical method for solving Fredholm integral equations of the second kind is only applicable when the covariance function is exponential, triangular and Wiener-Levy type. Phoon [26] proposed a Wavelet-Galerkin solution method that is not restricted by the type of covariance function.

When the random field area is [0, a], the mother wavelet function of Haar wavelet can be expressed as,

$$\psi(x) = \begin{cases} 1 & x\in[0,a/2) \\ -1 & x\in[a/2,a) \\ 0 & \text{other} \end{cases} \tag{43}$$

where the mother wavelet can generate a family of orthogonal Haar wavelets by shifting and scaling,

$$\psi_{j,k}(x) = \alpha_j\psi(2^j x-k) \qquad j,k\in Z \tag{44}$$

in which j controls the frequency domain, $k$controls the time domain, $\alpha_j$controls the amplitude. In this study, α_j is taken to be 1, then $\psi_{j,k}(x)$ is a series of orthogonal functions with unit amplitude.

A series of Haar wavelet basis functions based on the area [0, 1] are introduced,

$$\begin{cases} \psi_0(x) = 1 \\ \psi_i(x) = \psi_{j,k}(2^j x-k) \\ i = 2^j+k;\ k=0,1,\ldots,2^j-1;\ j=0,1,\ldots,m-1. \end{cases} \tag{45}$$

where m is the maximum wavelet level.

Since the wavelet basis functions are all orthogonal, their inner products satisfy,

$$\int_0^1 \psi_i(x)\psi_j(x)\mathrm{dx} = h_i\delta_{ij} \tag{46}$$

therefore, the orthogonal function system satisfies,

$$\int_0^1 \boldsymbol{\psi}\boldsymbol{\psi}^{\mathrm{T}} \mathrm{dx} = \boldsymbol{H} \tag{47}$$

$$\boldsymbol{H} = \begin{bmatrix} h_0 & \cdots & 0 \\ \vdots & \ddots & \vdots \\ 0 & \cdots & h_{N-1} \end{bmatrix} \tag{48}$$

where $N = 2^m$, $h_0 = a, \dots, h_i = 2^{-j}$, and the subscript is the same as in Eq. (45).

Therefore, the eigenfunction $f_k(x)$ is expanded with a wavelet basis function as,

$$f_k(x) = \sum_{i=0}^{N-1} d_i^{(k)} \psi_i(x) = \boldsymbol{\psi}^{\mathrm{T}} \boldsymbol{D}^{(k)} \tag{49}$$

where $D^{(k)}$ represents the eigenvector corresponding to the k -th order eigenfunction.

The normalized orthogonal vector is defined as,

$$\hat{\boldsymbol{\psi}} = \boldsymbol{H}^{-1/2}\boldsymbol{\psi} \tag{50}$$

then we have,

$$\int_0^1 \hat{\boldsymbol{\psi}}\hat{\boldsymbol{\psi}}^{\mathrm{T}} \mathrm{dx} = 1 \tag{51}$$

thus, Eq. (49) can be rewritten as,

$$f_k(x) = \boldsymbol{\psi}^T \boldsymbol{D}^{(k)} = \boldsymbol{\psi}^T \boldsymbol{H}^{-1/2} \boldsymbol{H}^{1/2} D^{(k)} = \hat{\boldsymbol{\psi}}^T \hat{\boldsymbol{D}}^{(k)} \tag{52}$$

The eigenvalues λ_k and eigenvectors $\widehat{\boldsymbol{D}}^{(k)}$ can be obtained by solving Eq. (53),

$$\lambda_k \hat{\boldsymbol{D}}^{(k)} = \hat{\boldsymbol{A}} \hat{\boldsymbol{D}}^{(k)} \tag{53}$$

where $\widehat{\boldsymbol{A}}$ needs to be obtained by solving the 2D wavelet transform of the covariance function.

The wavelet transform cannot be applied to a continuous signal thus it needs to be discretised. For the covariance function $C(x_1, x_2)$, assume a set of values $F(x_i, x_j)$, where

$$x_i = 2a(i+1)/2N,\ x_j = 2a(j+1)/2N,\ (i, j = 0, \dots, N-1) \tag{54}$$

Substituting $F(x_i, x_j)$ into $C(x_1, x_2)$ to obtain a matrix $\boldsymbol{A}$ with $N \times N$ orders. A certain row of $\boldsymbol{A}$ is a $1 \times N$ vector, which can be expressed as,

$$[a_{m,0} \quad a_{m,1} \quad \cdots \quad a_{m,k} \quad \cdots \quad a_{m,N-1}] \tag{55}$$

where $k = 0,1,2, \dots, N-1$. The vector is processed using an inverse binary tree, and then the nodal values in subsequent layers are computed as,

$$a_{j,k} = \frac{1}{2}\left(a_{j+1,2k} + a_{j+1,2k+1}\right) \tag{56}$$

where $k = 0,1,2,\ldots,2^j - 1$, and $j = m-1,\ldots,2,1,0$. The wavelet coefficients are evaluated from the nodal values in this binary tree as,

$$c_{j,k} = \frac{1}{2}\left(a_{j+1,2k+1} - a_{j+1,2k}\right) \tag{57}$$

Finally, the 1D wavelet transform of Eq. (55) is written,

$$[a_{0,0} \quad c_1 \quad \cdots \quad c_{N-1}] \tag{58}$$

in which,

$$\begin{cases} c_i = c_{j,k} \\ i = 2^j + k \\ k = 0,1,\ldots,2^j - 1 \\ j = 0,1,\ldots,m-1 \end{cases} \tag{59}$$

Applying a 1D wavelet transform to each row of the matrix $\boldsymbol{A}$, and then performing 1D wavelet transform to each column result in $\bar{\boldsymbol{A}}$; performing $\widehat{\boldsymbol{A}} = \boldsymbol{H}^{1/2}\bar{\boldsymbol{A}}\boldsymbol{H}^{1/2}$ on $\bar{\boldsymbol{A}}$ leads to the coefficient matrix $\widehat{\boldsymbol{A}}$. The eigenvalues and eigenvectors can be derived by substituting $\widehat{\boldsymbol{A}}$ into Eq. (53).

4.2 Modified point estimation method

Assuming that $g(\boldsymbol{\Gamma})$ is a function of the random vectors $\boldsymbol{\Gamma} = [\gamma_1, \gamma_2, \ldots, \gamma_N]^T$ and $p(\gamma)$ is the joint probability density of $\boldsymbol{\Gamma}$, the expectation and variance of $g(\boldsymbol{\Gamma})$ are,

$$E\left[g(\boldsymbol{\Gamma})\right] = \int_{-\infty}^{+\infty} g(\gamma)\, p(\gamma)\, \mathrm{d}\gamma \tag{60}$$

$$D\left[g(\boldsymbol{\Gamma})\right] = E\left[\left(g(\boldsymbol{\Gamma}) - \mu_{\boldsymbol{\Gamma}}\right)^2\right] = \int_{-\infty}^{+\infty} \left[g(\gamma) - \mu_{\boldsymbol{\Gamma}}\right]^2 p(\gamma)\, \mathrm{d}\gamma \tag{61}$$

where $\mu_{\boldsymbol{\Gamma}}$ is the expectation of $g(\boldsymbol{\Gamma})$.

Since $\boldsymbol{\Gamma}$ contains multiple random variables, the moments of $g(\boldsymbol{\Gamma})$ are difficult to be computed directly. According to the multivariate function decomposition method proposed by Xu and Rahman [40], an *n*-dimensional variational function can be approximated by the sum of multiple one-dimensional variational functions $g_i(\gamma_i)$,

$$\begin{cases} g(\boldsymbol{\Gamma}) \cong \sum_{i=1}^{N} g_i(\gamma_i) - (N-1)\, g(\boldsymbol{c}) \\ g_i(\gamma_i) = g(c_1, \cdots, c_{i-1}, \gamma_i, c_{i+1}, \cdots, c_N) \end{cases} \tag{62}$$

where $\boldsymbol{c} = [c_1, c_2, \cdots, c_N]^T$ is the vector of reference point and $g_i(\gamma_i)$ only depends on the variable γ_i.

Substituting Eq. (62) into Eqs. (60) and (61) respectively, the expectation and variance of $g(\boldsymbol{\Gamma})$ can be approximated as,

$$E\left[g\left(\boldsymbol{\Gamma}\right)\right] \cong E\left[\sum_{i=1}^{N} g_i\left(\gamma_i\right) - \left(N-1\right) g\left(\boldsymbol{c}\right)\right] = \sum_{i=1}^{N} E\left[g_i\left(\gamma_i\right)\right] - \left(N-1\right) g\left(\boldsymbol{c}\right) \quad (63)$$

$$\begin{aligned} D\left[g\left(\boldsymbol{\Gamma}\right)\right] &= E\left\{\left[g\left(\boldsymbol{\Gamma}\right) - \mu_{\boldsymbol{\Gamma}}\right]^2\right\} \cong E\left\{\sum_{i=1}^{n}\left[g_i\left(\gamma_i\right) - \mu_{\boldsymbol{\Gamma}}\right]^2 - \left(N-1\right)\left[g\left(c\right) - \mu_{\boldsymbol{\Gamma}}\right]^2\right\} \\ &= \sum_{i=1}^{n} E\left\{\left[g_i\left(\gamma_i\right) - \mu_{\boldsymbol{\Gamma}}\right]^2\right\} - \left(N-1\right)\left[g\left(c\right) - \mu_{\boldsymbol{\Gamma}}\right]^2 \end{aligned} \quad (64)$$

If the random variables in the function $g_i(\gamma_i)$ obey a standard Gaussian distribution, $E[g_i(\gamma_i)]$ and $E[(g_i(\gamma_i) - \mu_{\boldsymbol{\Gamma}})^2]$ can be approximated by the Gaussian-Hermite integral function as [39],

$$E\left[g_i\left(\gamma_i\right)\right] = \sum_{l=1}^{r} \frac{\omega_{GH,l}}{\sqrt{\pi}} g_i\left(\sqrt{2}\gamma_{GH,l}\right) \quad (65)$$

$$E\left\{\left[g_i\left(\gamma_i\right) - \mu_{\boldsymbol{\Gamma}}\right]^2\right\} = \sum_{l=1}^{r} \frac{\omega_{GH,l}}{\sqrt{\pi}} \left[g_i\left(\sqrt{2}\gamma_{GH,l}\right) - \mu_{\boldsymbol{\Gamma}}\right]^2 \quad (66)$$

where r represents the number of estimating points of a Gaussian-Hermite integration; $\gamma_{GH,l}$ and $\omega_{GH,l}$ are the abscissa and weight for the Gaussian-Hermite integration, respectively.

4.3 Stochastic response estimation

The Gaussian random field remain one of the most commonly utilized stochastic models in current research [35]. Given the absence of prior investigations into random field of ceramic-metal FGSNPs, the elastic modulus of ceramics and metals (E_{c} and E_{m}) are treat as stationary homogeneous Gaussian random fields for stochastic analysis in this study, which are expanded using the KLE as,

$$E_{\mathrm{c}}(x) = \bar{E}_{\mathrm{c}}(x) + \sum_{i=1}^{N} \gamma_i \sqrt{\lambda_i} f_i\left(x\right) \quad (67)$$

$$E_{\mathrm{m}}(x) = \bar{E}_{\mathrm{m}}(x) + \sum_{i=1}^{N} \gamma_i \sqrt{\lambda_i} f_i\left(x\right) \quad (68)$$

In Eqs. (67) and (68), the uncertainties in material properties are characterized by the random variables γ_i. Let $\boldsymbol{\Gamma} = [\gamma_1, \gamma_2, \ldots, \gamma_N]^T$represent an *n*-dimensional random vectors including these random variables. Then Eq. (31) is rewritten as,

$$\boldsymbol{K}(\boldsymbol{\Gamma})\boldsymbol{U}(\boldsymbol{\Gamma}) = \boldsymbol{F} \tag{69}$$

where $\boldsymbol{K}(\boldsymbol{\Gamma})$ is the random stiffness matrix and $\boldsymbol{U}(\boldsymbol{\Gamma})$ denotes random displacement (response) vector of the structure, which is solved by the following equation,

$$\boldsymbol{U}(\boldsymbol{\Gamma}) = \boldsymbol{K}(\boldsymbol{\Gamma})^{-1}\boldsymbol{F} \tag{70}$$

Thus, the stochastic static response of the structure is evaluated by solving the mean and variance of the stochastic stiffness matrix. According to Eqs. (60)-(66), the expectation and variance of $\boldsymbol{K}(\boldsymbol{\Gamma})$ can be computed as,

$$\mu_{\boldsymbol{K}} \approx \sum_{i=1}^{N}\sum_{l=1}^{r}\frac{\omega_{GH,l}}{\sqrt{\pi}} K_{i,l}\left(\gamma_{i,l}\right) - \left(N-1\right)K\left(\boldsymbol{c}\right) \tag{71}$$

$$\begin{cases} \mathrm{var}_{\boldsymbol{K}} = \sum_{i=1}^{N}\sum_{l=1}^{r}\frac{\omega_{GH,l}}{\sqrt{\pi}}\left[R_{i,l}\left(\gamma_{i,l}\right) - \mu_{\boldsymbol{K}}\right]^2 - \left(N-1\right)\left[K\left(\boldsymbol{c}\right) - \mu_{\boldsymbol{K}}\right]^2 \\ Std.D_{\boldsymbol{K}} = \sqrt{\mathrm{var}_{\boldsymbol{K}}} \end{cases} \tag{72}$$

where, $\mu_{\boldsymbol{K}}, \mathrm{var}_{\boldsymbol{K}}$ and $Std.D_{\boldsymbol{K}}$ are the mean, variance and standard deviation of $\boldsymbol{K}(\boldsymbol{\Gamma})$, respectively. $K_{i,l}\left(\gamma_{i,l}\right)$ denotes the l-th estimation point of the i-th random variable, and $\gamma_{i,l} = \left[\gamma_c, \gamma_c, \cdots, \sqrt{2}\gamma_{GH,l}, \cdots, \gamma_c, \gamma_c\right]$ denotes that all the variables are γ_c, except for the i-th variable which is $\sqrt{2}\gamma_{GH,l}$. The $\boldsymbol{c}$ of $K(\boldsymbol{c})$ is the reference point vector, which can be written as $\boldsymbol{c} = [\gamma_c, \gamma_c, \cdots, \gamma_c, \gamma_c]$. When the reference point $\boldsymbol{c} = [0,0,\cdots,0,0]$, we have,

$$K_{i,l}\left(\gamma_{i,l}\right) = K_{i,l}\left(\left[0,0,\cdots,\sqrt{2}\gamma_{GH,l},\cdots 0,0\right]\right) \tag{73}$$

$$K\left(\boldsymbol{c}\right) = K\left(\left[0,0,\cdots,0,\cdots 0,0\right]\right) \tag{74}$$

The sample of the material elastic modulus for the l-th estimating point of the i-th variable that is associated with $K_{i,l}\left(\gamma_{i,l}\right)$ and $K(\boldsymbol{c})$ is expressed as,

$$E_{K,il}(x) = \bar{E}_K(x) + \sqrt{2}\gamma_{GH,l}\sqrt{\lambda_i}\, f_i(x) \tag{75}$$

$$E_{K,c}(x) = \bar{E}_K(x) \tag{76}$$

therefore, $K_{i,l}\left(\gamma_{i,l}\right)$ and $K(\boldsymbol{c})$ in Eqs. (71) and (72) can be obtained by adopting $E_{K,il}$ from Eq. (75) and $E_{K,c}$ from Eq. (76), respectively, and thus the mean and the variance of displacements and stress will be found finally.

As a result, a novel stochastic meshfree computational framework of MEPEM-RPIM was developed. Initially, the governing equation of plates are deduced employing the HSDT-based RPIM meshfree method, and then the mean and variance of stochastic static response are computed through the MPEM.

5. Numerical examples and discussions

To compute the integrals, boundary conditions are imposed on the governing equations, and the common boundary conditions are shown in Table 1. Unless otherwise specified, a square simply supported (SSSS) plate with a width-to-thickness ratio of $a/h = 10$ is employed in this paper, whose material parameters are set to: $E_\mathrm{m} = 70$ GPa, $E_\mathrm{c} = 151$ GPa, $\rho_\mathrm{m} = 2700$ kg/m^3, $\rho_\mathrm{c} = 5680$ kg/m^3, $\nu_\mathrm{m} = \nu_\mathrm{c} = 0.3$. In addition, the normalisation parameters for all numerical results analysis are evaluated in the following form

- Dimensionless central deflection:

$$\bar{w} = \frac{10hE_0}{a^2 q_0} w\left(\frac{a}{2}, \frac{b}{2}, \bar{z}\right) \tag{77}$$

where$E_0 = 1$ Gpa.

- Dimensionless axial stress:

$$\bar{\sigma}_{xx} = \frac{h^2}{a^2 q_0} \sigma_{xx}\left(\frac{a}{2}, \frac{b}{2}, \bar{z}\right) \tag{78}$$

- Dimensionless shear stress:

$$\bar{\tau}_{xz} = \frac{h}{a q_0} \tau_{xz}\left(0, \frac{b}{2}, \bar{z}\right) \tag{79}$$

Table 1. The boundary conditions for plates.

Type	Conditions	Values
SSSS	At $y = 0, b$ At $x = 0, a$	$u = w_0 = \beta_x = \phi_x = 0$ $v = w_0 = \beta_y = \phi_y = 0$
CCCC	At all edges	$u = v = w_0 = \beta_x = \beta_y = \phi_x = \phi_y = 0$
SCSC	At $y = 0, b$ At $x = 0, a$	$u = v = w_0 = \beta_x = \beta_y = \phi_x = \phi_y = 0$ $v = w_0 = \beta_y = \phi_y = 0$
CSCS	At $y = 0, b$ At $x = 0, a$	$u = w_0 = \beta_x = \phi_x = 0$ $u = v = w_0 = \beta_x = \beta_y = \phi_x = \phi_y = 0$

5.1 Verification and comparison

Initially, in order to estimate the influence of scale factor α_c for dimensionless size of the support domain, the term α_c has been chosen from 2.0 to 3.0 as suggested by Liu et al. [62]. The obtained results are depicted in Table 2 and compared with the analytical solution of Reddy et al. [55] based on the third-order shear deformation theory. It is clear that the minimum error occurs at $\alpha_c = 2.4$. Therefore, the scale factor α_c can be fixed at 2.4 for all of following problems to cover the large enough nodes in the support domain for constructing shape functions and achieving high accuracy in solutions.

Table 2 The normalized deflection of isotropic square plate under a uniformly distributed load (*a/h* = 10) with a range of α_c values.

α_c	Reddy [55] TSDT	RPIM-HSDT		α_c	Reddy [55] TSDT	RPIM-HSDT	
	$\bar{w}$	$\bar{w}$	$\Delta\bar{w}(\%)$		$\bar{w}$	$\bar{w}$	$\Delta\bar{w}(\%)$
	4.666				4.666		
2.0		4.7156	1.06%	2.6		4.6488	-0.37%
2.1		4.7018	0.77%	2.7		4.6429	-0.50%
2.2		4.7002	0.73%	2.8		4.6314	-0.74%
2.3		4.6819	0.34%	2.9		4.6303	-0.77%
2.4		4.6684	0.05%	3.0		4.6299	-0.77%
2.5		4.6584	-0.16%				

Table 3 Comparison of dimensionless central deflection of FGSNP-A with those of Zenkour et al. [63].

p	Source	Type			
		1-1-1	2-1-2	1-2-1	2-2-1
1	Zenkour(CLPT)	0.28026	0.29417	0.25958	0.26920
	Zenkour(FSDT)	0.29301	0.30750	0.27167	0.28168
	Zenkour(TSDT)	0.29199	0.30632	0.27090	0.28085
	Present	**0.29011**	**0.30450**	**0.27076**	**0.28076**
2	Zenkour(CLPT)	0.32067	0.33942	0.29095	0.30405
	Zenkour(FSDT)	0.33441	0.35408	0.30370	0.31738
	Zenkour(TSDT)	0.33289	0.35231	0.30263	0.31617
	Present	**0.33164**	**0.35104**	**0.30187**	**0.31541**
5	Zenkour(CLPT)	0.35865	0.37789	0.32283	0.33693
	Zenkour(FSDT)	0.37356	0.39418	0.33631	0.35123
	Zenkour(TSDT)	0.37145	0.39183	0.33480	0.34960
	Present	**0.37088**	**0.39104**	**0.33456**	**0.34822**
10	Zenkour(CLPT)	0.37236	0.38941	0.33612	0.34915
	Zenkour(FSDT)	0.38787	0.40657	0.34996	0.36395
	Zenkour(TSDT)	0.38551	0.40407	0.34824	0.36215
	Present	**0.38517**	**0.40333**	**0.34823**	**0.36188**

Table 4 Comparison of dimensionless axial stress and shear stress of FGSNP-A with those of Zenkour et al. [63].

p	Source	Type							
		1-1-1		2-1-2		1-2-1		2-2-1	
		$\bar{\sigma}_{xx}(h/2)$	$\bar{\tau}_{xz}(0)$	$\bar{\sigma}_{xx}(h/2)$	$\bar{\tau}_{xz}(0)$	$\bar{\sigma}_{xx}(h/2)$	$\bar{\tau}_{xz}(0)$	$\bar{\sigma}_{xx}(h/2)$	$\bar{\tau}_{xz}(0)$
1	Zenkour(CLPT)	1.38303	0.23257	1.45167	0.24316	1.28096	0.22057	1.27749	0.22762
	Zenkour(FSDT)	1.42617	0.26117	1.49587	0.27104	1.32309	0.25258	1.32062	0.25951
	Zenkour(TSDT)	1.42892	0.26809	1.49859	0.27774	1.32590	0.26004	1.32342	0.26680
	Present	**1.41253**	**0.27022**	**1.48463**	**0.28399**	**1.30872**	**0.26966**	**1.30737**	**0.28173**
2	Zenkour(CLPT)	1.58242	0.25077	1.67496	0.26752	1.43580	0.23257	1.42528	0.24316
	Zenkour(FSDT)	1.62748	0.27188	1.72144	0.28838	1.47988	0.25834	1.47095	0.26939
	Zenkour(TSDT)	1.63025	0.27807	1.72412	0.29422	1.48283	0.26543	1.47387	0.27627
	Present	**1.61521**	**0.28257**	**1.71165**	**0.29967**	**1.46615**	**0.27752**	**1.45898**	**0.29984**
5	Zenkour(CLPT)	1.76988	0.27206	1.86479	0.29731	1.59309	0.24596	1.56401	0.26099
	Zenkour(FSDT)	1.81580	0.28643	1.91302	0.31454	1.63814	0.26512	1.61181	0.28265
	Zenkour(TSDT)	1.81838	0.29150	1.91547	0.31930	1.64106	0.27153	1.61477	0.28895
	Present	**1.80620**	**0.30108**	**1.90525**	**0.32743**	**1.62619**	**0.28780**	**1.60181**	**0.31978**
10	Zenkour(CLPT)	1.83754	0.28299	1.92165	0.31316	1.65844	0.25257	1.61645	0.26998
	Zenkour(FSDT)	1.88376	0.29566	1.97126	0.33242	1.70417	0.26895	1.66660	0.29080
	Zenkour(TSDT)	1.88147	0.29529	1.97313	0.33644	1.64851	0.27676	1.61979	0.29671
	Present	**1.87540**	**0.30976**	**1.96372**	**0.34393**	**1.69304**	**0.29141**	**1.67612**	**0.32638**

Next, the central deflections, axial stresses and shear stresses of the plates are computed for different sandwich configurations as well as varying power-law exponents p, as listed in Tables 3 and 4. Comparison with the analytical solution of Zenkour et al. [63] verifies the correctness of the governing equations developed based on RPIM. It was observed that increasing p leads to greater plate's central deflection and axial stress at the top centre point. This occurs because an increase in p reduces the ceramic content in the surface of the FGSNP-A, resulting in decreased stiffness and increased deflection, which concentrates stresses in localized areas. Moreover, Fig. 5 shows the variation of axial stress with thickness for FGSNPs, while Fig. 6 presents the variation of shear stress, from which we can notice that the variation curves of stresses exhibit 'folded corners' at the interface between the core and surface layers as p increases. The larger the value of p, the more pronounced this effect. This is attributed to the fact that an increase in p leads to either a decrease (for FGSNP-A) or an increase (for FGSNP-B) in the ceramic content of the surface layers of FGSNPs, accentuating the stiffness difference between the core and surface layers and thus causing an abrupt interfacial stress change. The correctness of Figs. 5 and 6 is validated by comparing the results with those of FGSNPs obtained by Daikh et al. [52] using an analytical solution. These comparative analyses further demonstrate that the computational framework and procedures developed in this paper using RPIM are reliable and efficient, effectively replacing analytical methods.

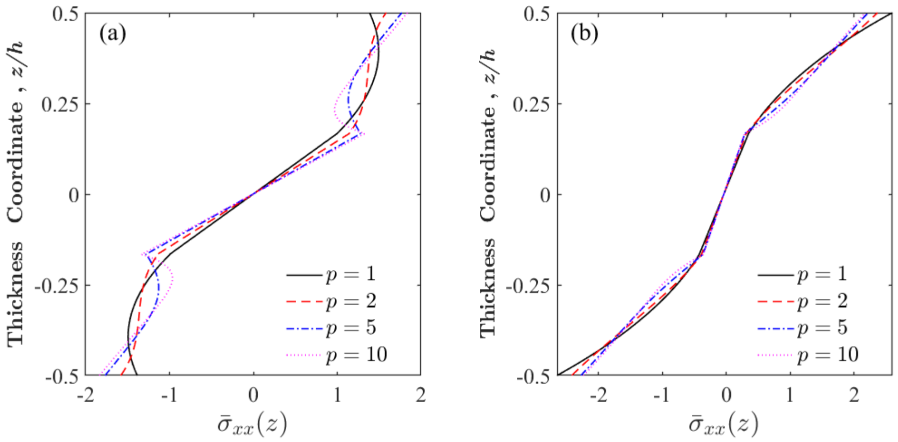

Fig. 5 Dimensionless axial stresses along the thickness of 1-1-1 FGSNPs: (a) FGSNP-A; (b) FGSNP-B.

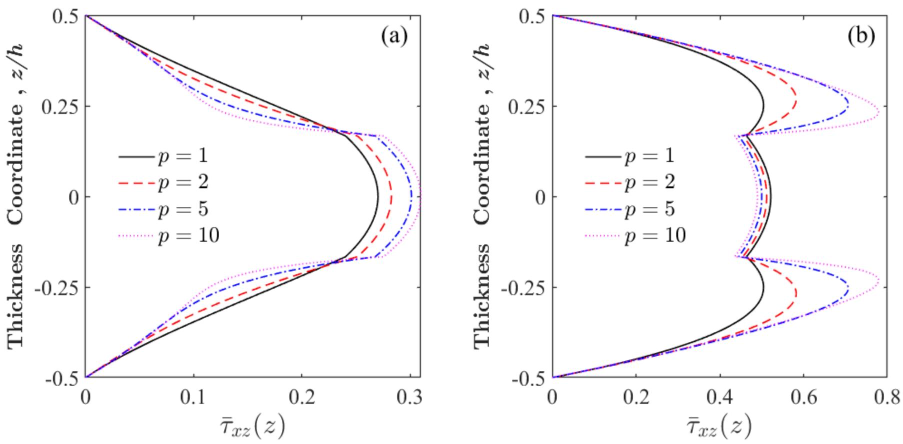

Fig. 6 Dimensionless shear stresses along the thickness of 1-1-1 FGSNPs: (a) FGSNP-A; (b) FGSNP-B.

Table 5 The parameters of the random fields.

Stochastic structural parameters	Values	Region	Correlative length	Type
E_c	151 Gpa	$0 \le x \le L_x = a$ $0 \le y \le L_y = b$	$c_x = 0.5L_x$ $c_y = 0.5L_y$	Gaussian
E_m	70 Gpa	$0 \le x \le L_x = a$ $0 \le y \le L_y = b$	$c_x = 0.5L_x$ $c_y = 0.5L_y$	Gaussian

5.2 Stochastic analysis

5.2.1 Using KLE method to discretize random fields

Given the spatial variability of material parameters, the elastic modulus of ceramics and metals (E_c and E_m) are treated as smooth uniform Gaussian random fields in this study, respectively. Table 5 provides relevant parameters of the random fields. Taking a 1D random field (random field length $L = 6$, correlative length $c = 0.5L$, coefficient of variation $c_v = 0.05$) as an example, the first four eigenfunctions of exponential covariance function for analytical method are given by Eq. (41), as shown in Eq. (80). Fig. 7 illustrates the simulation results by Wavelet-Galerkin method. Comparing with analytical solution, it can be observed that simulation accuracy improves with the increase of the maximum wavelet level m. To strike a balance between simulation accuracy and computational cost, we set ‘ $m = 7$’ for this study.

$$\begin{cases} f_1(x) = \dfrac{1}{\sqrt{\dfrac{(0.2868^2 \times c^2 + 1)L}{2} + c}}\left[0.2868c\cos(0.2868x) + \sin(0.2868x)\right] \\ f_2(x) = \dfrac{1}{\sqrt{\dfrac{(0.6763^2 \times c^2 + 1)L}{2} + c}}\left[0.6763c\cos(0.6763x) + \sin(0.6763x)\right] \\ f_3(x) = \dfrac{1}{\sqrt{\dfrac{(1.1419^2 \times c^2 + 1)L}{2} + c}}\left[1.1419c\cos(1.1419x) + \sin(1.1419x)\right] \\ f_4(x) = \dfrac{1}{\sqrt{\dfrac{(1.6377^2 \times c^2 + 1)L}{2} + c}}\left[1.6377c\cos(1.6377x) + \sin(1.6377x)\right] \end{cases} \tag{80}$$

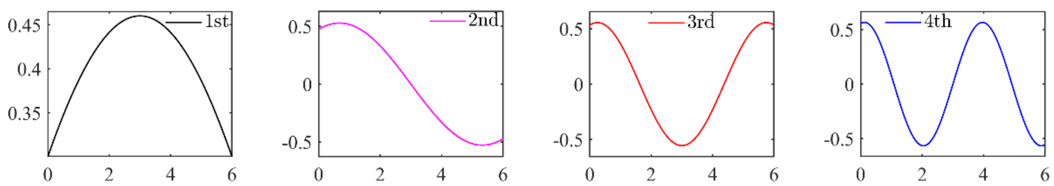

(a) Analytical solution

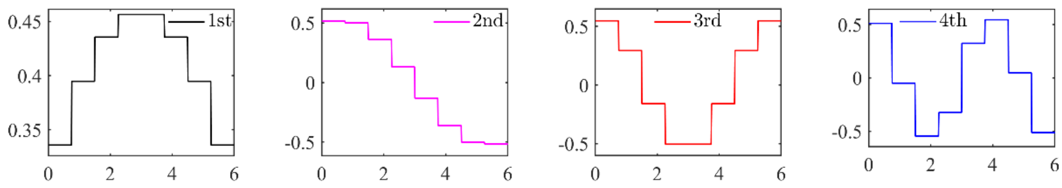

(b) Numerical solution by Wavelet-Galerkin method (m=3)

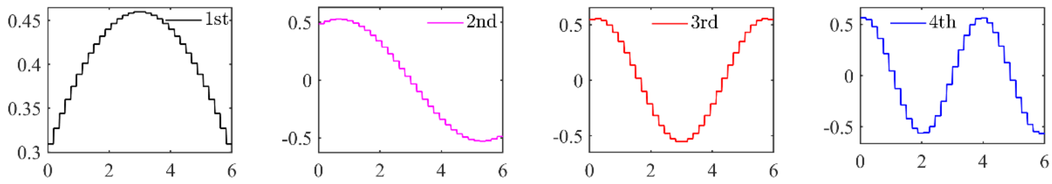

(c) Numerical solution by Wavelet-Galerkin method (m=5)

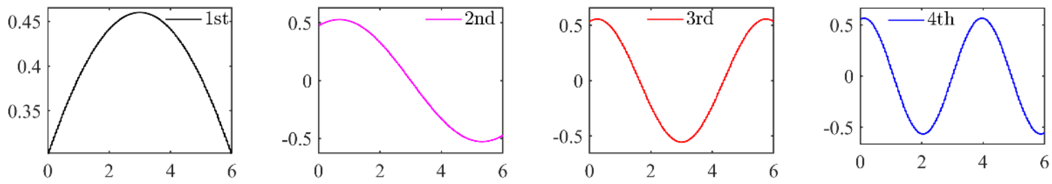

(d) Numerical solution by Wavelet-Galerkin method (m=7)

Fig. 7 The first four eigenfunctions computed by analytical method and Wavelet-Galerkin method.

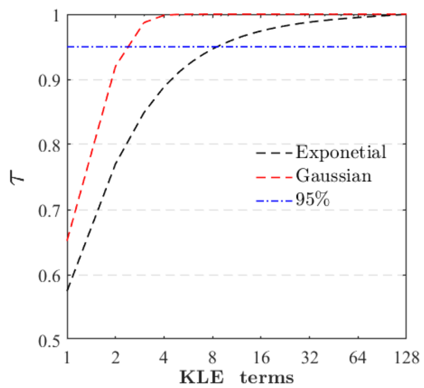

Fig. 8 The growth of index τ_{Guassian} and $\tau_{\text{Exponential}}$ with the increase of the truncating KLE term number.

Although the analytical method provides exact solutions, it is limited to solving transcendental equations and can only be applied to specific covariance functions. In addition, there is a notable difference in truncating KLE terms between Exponential and Gaussian covariance functions due to the different decay rates of their eigenvalues. The following exponent τ is utilised to assess the completeness of simulating random fields with different covariance functions [19].

$$\tau = \frac{\sum_{i=1}^{N} \lambda_i}{\Omega \sigma^2} \tag{81}$$

where Ω is a random region. In present study, KLE terms are truncated when τ

reaches 95%. Substituting the eigenvalues into Eq. (81), the growth of τ_{Guassian} and $\tau_{\text{Exponential}}$ with increasing truncation number $N = 2^m$ is shown in Fig. 8. It is clear that the decay rate of Gaussian's eigenvalues is significantly faster than that of Exponential, indicating that fewer KLE terms are needed for the Gaussian covariance function to simulate random fields, resulting in considerable computational cost savings.

It is worth noting that the Gaussian random fields E_{c} and E_{m} in this investigation belong to 2D random fields. The 2D random field with regular shape can be decomposed into 1D random fields in two directions for the KLE, as described in [19]. Therefore, the covariance function of 2D random field $C(x_1, x_2; y_1, y_2)$ can be decomposed into 1D random fields in x direction with $C(x_1, x_2)$ and y direction with $C(y_1, y_2)$. Then solving the Fredholm integral equations respectively to obtain the eigenvalues λ_m^x, λ_n^y and eigenfunctions $f_m^x(x)$, $f_n^y(y)$, and combing them to form the 2D eigenvalues and eigenfunctions as follows.

$$\lambda_i = \frac{\lambda_m^x \lambda_n^y}{\sigma^2} \tag{82}$$

$$f_i(x, y) = f_m^x(x) f_n^y(y) \tag{83}$$

Fig. 9 displays the shape of the first four eigenfunctions for a 2D random field. Here, $[i, j]$ represents the combination of the i-th eigenfunction in direction x with the j-th eigenfunction in direction y. By now, we have investigated the characteristics of covariance functions for random fields and illustrated the KLE method.

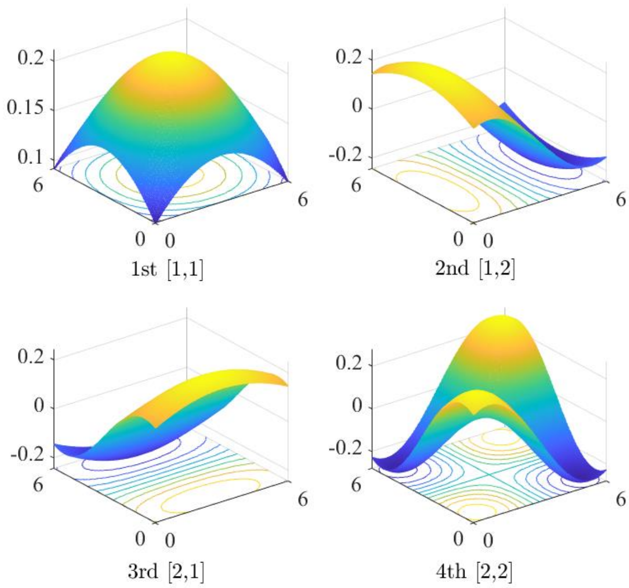

Fig. 9 The first four eigenfunctions of the 2D random field with exponential covariance function.

5.2.2 Stochastic static analysis for FGSNPs

To verify the correctness of MPEM-RPIM, Monte Carlo simulation (MCS) with a sample size of 10,000 is performed on the same stochastic structure. Taking the random field E_c of FGSNP-A as an example, Fig. 10 compares the mean and standard deviation of plate's central deflection computed by MCS and MPEM, respectively. The results show that both two methods produce nearly identical outcomes, indicating that MPEM-RPIM is a reliable stochastic computational method. Moreover, Table 6 provides the CPU time required for computation using these two methods. The presented method requires only about 1/740th of the time needed by MCS. Therefore, it can be concluded that, under the same computational conditions, the novel stochastic meshfree computational framework developed in this paper significantly reduces computational time and thus saves computational costs.

Table 6 Comparison of CPU time of MCS and MPEM.

c_v	MCS	MPEM	c_v	MCS	MPEM
0.05	38643.5437	52.2834	0.20	38714.4581	52.3473
0.10	38552.6485	52.1677	0.25	38561.3267	52.2461
0.15	38586.5561	52.2054	0.30	38629.7461	52.2294
			Mean	38614.7132	52.2466

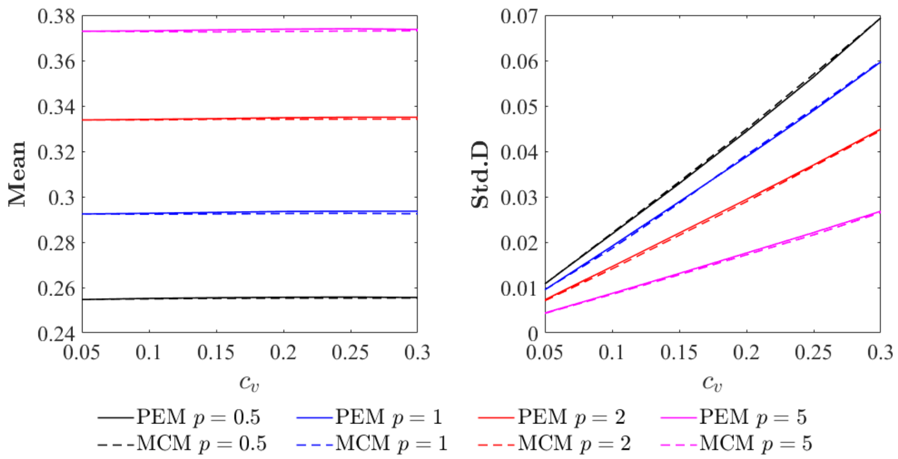

Fig 10 Comparison of mean and standard deviation of dimensionless central deflection of 1-1-1 FGSNP-A subjects to random field E_c computed by MCS and NPEM.

As the second stochastic comparison example, the validation of deflection statics of N_i/Al_2O_3 FGM plate with power-law exponents $p = 2$ and thickness ratio $a/h = 10$ is presented. Elastic modulus of metal E_m is considered to be independent random variable. Fig. 11 demonstrates that the result obtained by present method agrees fairly well with those reported by Tomar et al. [64] using the first-order perturbation technique and Yang et al. [65] using the semi-analytical method. This further validates the correctness of MPEM-RPIM.

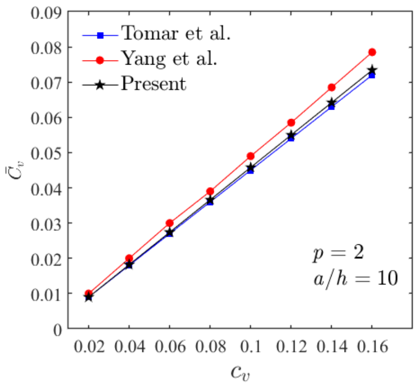

Fig. 11 Comparison of the coefficient of variation $\bar{C}_v$ of central deflection of *N_i/Al_2O_3* FGM plate

After validation, the developed stochastic meshfree computational framework is utilized for the static bending analysis of structures to determine the stochastic response sensitivity of FGSNPs. In this research, the spatial coefficients of variation c_v for the random fields E_c and E_m are taken to be in the range of 0.005 to 0.3, while the coefficient of variation $\bar{C}_v$ (*Std.D/Mean*) for the stochastic response of the structure is used to assess its sensitivity to the random fields.

Fig. 12 illustrates the effects of the random field E_c on FGSNPs, showing that $\bar{C}_v$ of central deflection increases as c_v increases, indicating an augmentation in sensitivity of plates with heightened spatial variability of materials. Furthermore, compared to FGSNP-B, random field E_c has a greater effect on FGSNP-A, while the structures with larger power-law exponent p are subjected to lower the effects. This is because FGSNP-A has a higher ceramic content than that of FGSNP-B, making it more susceptible to the random field E_c. Conversely, increasing power-law exponent reduces the ceramic content, which mitigates the adverse effects. In contrast, Fig. 13 shows that for the random field E_m, FGSNP-B is more significantly affected, with effects increasing as the power-law exponent increases. This is due to FGSNP-B's metal core layer and the opposing distribution of ceramic volume percentage compared to FGSNP-A, which leads them to manifest two completely contrasting material properties. Notably, the maximum $\bar{C}_v$ of central deflection of FGSNP-A is lower than that of FGSNP-B, which can be attributed to the higher elastic modulus of ceramics, providing greater stability to FGSNP-A.

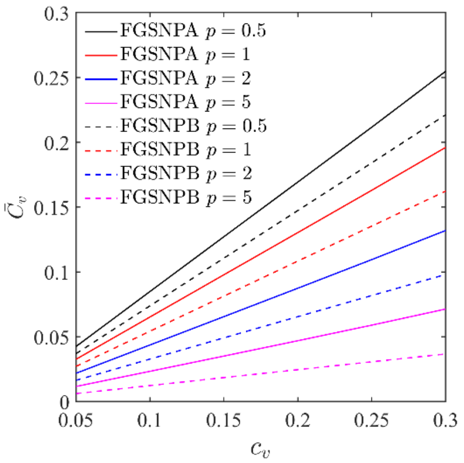

Fig. 12 Effect of random fields E_c on the dimensionless central deflection of 1-1-1 FGSNPs with different power-law exponent *p*.

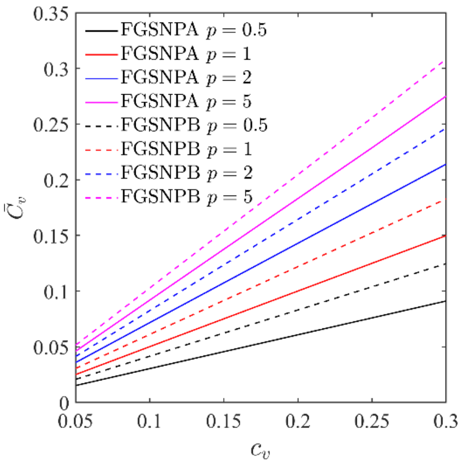

Fig. 13 Effect of random fields E_m on the dimensionless central deflection of 1-1-1 FGSNPs with different power-law exponent *p*.

The standard deviation of deflection curves is depicted in Fig. 14 to reveal the effects of random field E_c on the FGSNP-A with different sandwich configurations and power-law exponents. Observing the figure, it becomes apparent that the thicker core layer, the more FGSN-A is affected by random field E_c, whereas an increase in the power-law exponent diminishes this effect. This arises because FGSNP-A has a ceramic core layer, and increasing its thickness raises the ceramic content, which enhances the sensitivity of structures to random field E_c. In addition, the effects of random field E_c on the FGSNP-B with different sandwich configurations are illustrated in Fig. 15. Comparing Figs. 14 and 15, we can obtain the opposite conclusions. Furthermore, it can be anticipated that the impact of random field E_m on the stochastic deflection of FGSNPs will yield conclusions opposite to those drawn for random field E_c .

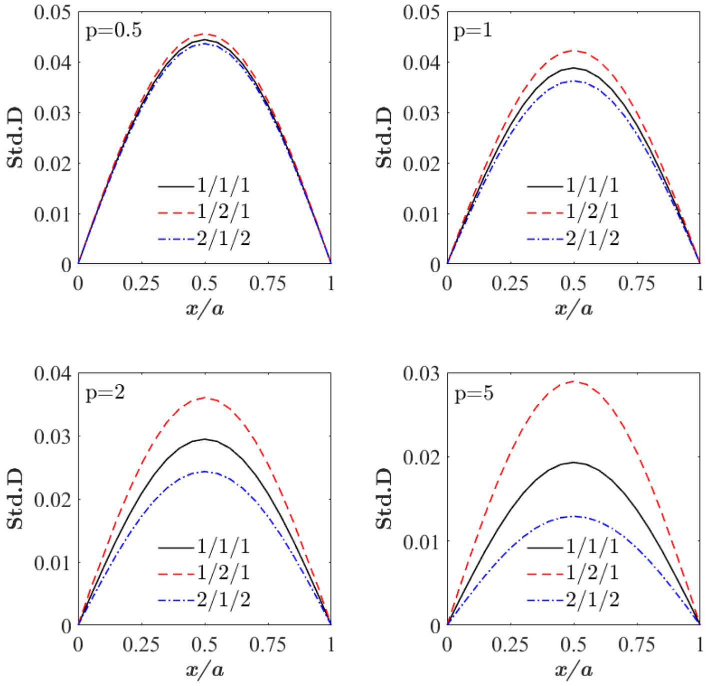

Fig. 14 Effect of random field E_c on the dimensionless deflection curve at $(x, y = b/2)$ of FGSNP-A with different sandwich configurations and power-law exponent p.

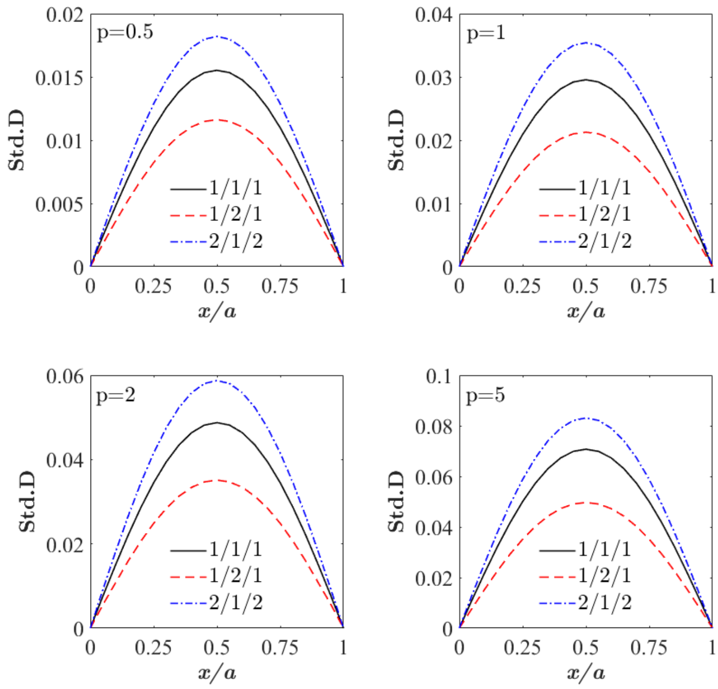

Fig 15 Effect of random field E_c on the dimensionless deflection curve at $(x, y = b/2)$ of FGSNP-B with different sandwich configurations and power-law exponent p.

For further examination of stochastic static response, we plotted stochastic bands to better visualize the effect of random field fluctuations on the structural stresses. The stochastic bandwidth was determined using the Chebyshev inequality, which can be expressed as follows:

$$P\{|\bar{\omega}-\bar{\mu}|\geq\varepsilon\}\leq\frac{\sigma^2}{\varepsilon^2} \tag{84}$$

According to the above equation, the stochastic bandwidth with a confidence level of 95% contains 4.5 standard deviations, that is, the stochastic bandwidth is set to $\bar{\mu}\pm 4.5\sigma$, where $\bar{\mu}$ and σ are the mean and standard deviation, respectively.

The maximum stress in static analysis significantly influences structural damage, and thus it is necessary to examine effects of stochastic material parameters on the maximum stress. The stochastic bands depicting maximum axial and shear stresses of FGSNPs affected by random field E_{c} are illustrated in Figs. 16-19.

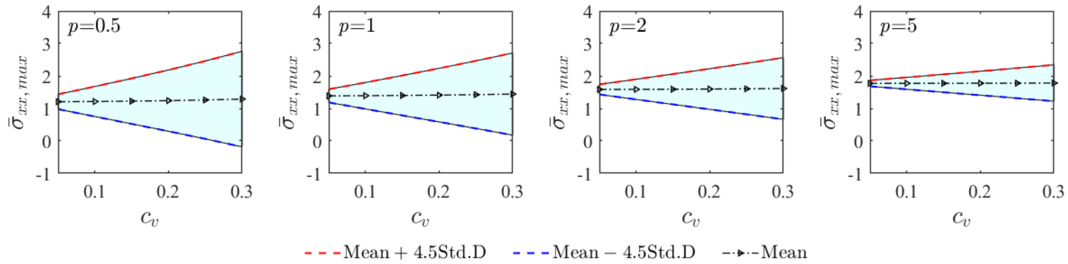

Fig. 16 Effect of random field E_c on the maximum dimensionless axial stress of 1-1-1 FGSNP-A with different power-law exponent p.

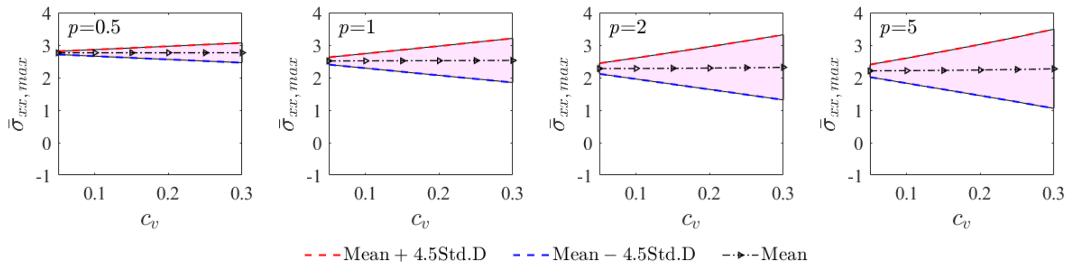

Fig. 17 Effect of random field E_c on the maximum dimensionless axial stress of 1-1-1 FGSNP-B with different power-law exponent p.

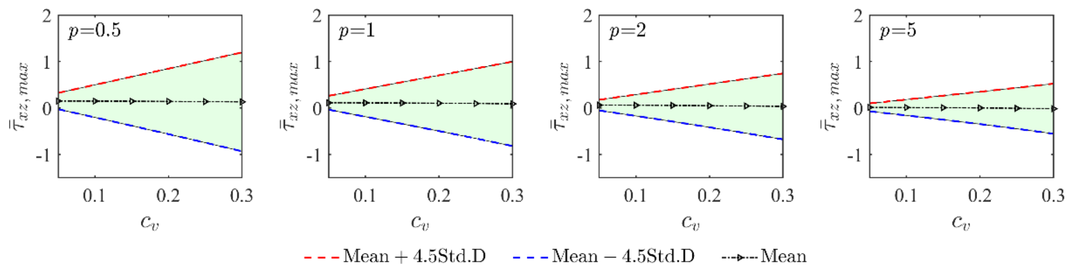

Fig. 18 Effect of random field E_c on the maximum dimensionless shear stress of 1-1-1 FGSNP-A with different

power-law exponent *p*.

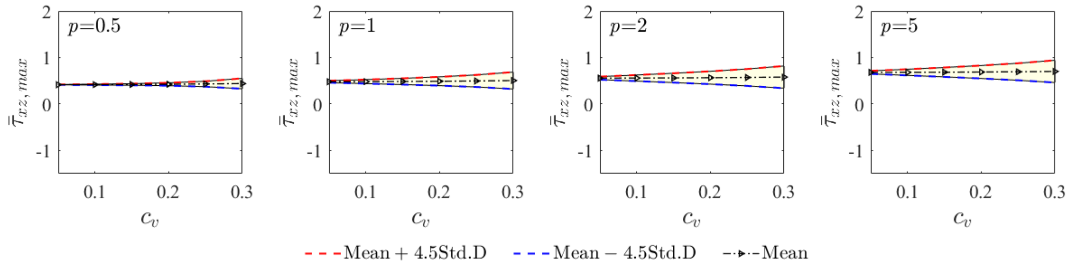

Fig. 19 Effect of random field E_c on the maximum dimensionless shear stress of 1-1-1 FGSNP-B with different power-law exponent *p*.

It is evident that the stochastic bandwidth increases with the growth of c_v, indicating a more pronounced stochastic response of structures as random field fluctuates. When comparing FGSNP-A and FGSNP-B, it is observed that the stochastic bandwidth of both axial and shear stresses decreases with an increase in p for FGSNP-A, while the opposite holds for FGSNP-B. This phenomenon occurs because an increase in p diminishes the ceramic content in FG surface layer of FGSNP-A, thereby reducing the impact of random field E_c on stresses. Conversely, the ceramic content in FG surface layer of FGSNP-B rises with an increase in p, making it more susceptible to random field E_c, which leads to a larger stochastic bandwidth. Importantly, we found that the stochastic bandwidths of shear stresses are all narrower than those of axial stresses, with FGSNP-B showing particularly pronounced. This can be explained by the fact that since the maximum axial stresses are acquired at the top/bottom surface of FGSNPs, the variation of ceramic percentage in FG surface layer further exacerbates the effect of random field E_c on the stress. In contrast, the maximum shear stress at the intermediate layer or demarcation benefits from the single stable material properties of core layer, mitigating the effect of random field. Particularly, the effect of random field E_c on shear stress of FGSNP-B, which has a metal core layer, is extremely weak.

6. Conclusion

In this study, we develop a novel stochastic computational framework that integrates the capabilities of MPEM and RPIM for addressing the stochastic static response of FGSNPs. The spatial variability of material parameters is introduced into elastic modulus of ceramic and metal, which are considered as random fields. To compute the mean and standard deviation of stochastic static response, the random fields are discretized by KLE method and then the obtained random variables are substituted into MPEM-RPIM for further computation. This framework has been demonstrated to be effective and robust, and the following conclusions can be drawn based on the analysis of numerical examples:

- The computational framework of MPEM-RPIM enables accurate and efficient computation for the stochastic static response of plate structures. It demonstrates higher efficiency compared to MCS method, substantially reducing computation time and cost.

- Compared to random field E_{m}, the stochastic static deflection of FGSNP-A becomes more sensitive to random field E_{c}, while the opposite is true for FGSNP-B. Notably, FGSNP-A exhibits higher stability than FGSNP-B concerning the impact of stochastic material parameters.
- Increasing coefficient of variation c_v exacerbates the fluctuation of random fields, leading to a more sensitive performance in the stochastic response of structures. Furthermore, enlarging power-law exponent diminishes the impact of random field E_{c} on FGSNP-A, while enhances its effect on FGSNP-B.
- The stochastic bands show that the maximum shear stress of FGSNPs is less affected by the random fields compared to the maximum axial stress. Particularly, the effect of random field E_{m} on the maximum shear stress of FGSNP-B is extremely weak.

Due to space limitations, only the sensitivity analysis of static stochastic response is performed in this paper. However, the developed stochastic computational framework can be extended to stochastic analysis of plates subject to impact loads, forced vibration, moving loads, etc., to investigate the effect of material uncertainty on structural response and optimise the structural design.

Acknowledgements

This work was funded by the Key R&D Projects of Hunan Province (No.2024AQ2018), the open fund of Shanghai High Performance Fibers and Composites Center and Center for Civil Aviation Composites, Donghua University, 2024, the 2023 Hunan Province Transportation Science and Technology Progress and Innovation Project (202305), the Henan Province Science and Technology Key Research Project (242102521034), the Hunan Provincial Natural Science Foundation Project (No. 2024JJ9067), Key Scientific Research Project of Hunan Provincial Department of Education, Project (21A0073), Taishan Program (tsqn202306278).

Declaration of Competing Interest

The authors declare that they have no known competing financial interests or personal relationships that could have appeared to influence the work reported in this paper.

Data Availability Statement

The data that support the findings of this study are available from the corresponding author, upon reasonable request.

References

[1] P. Phung-Van, A.J.M. Ferreira, H. Nguyen-Xuan, C.H. Thai, A nonlocal strain gradient isogeometric nonlinear analysis of nanoporous metal foam plates, Eng. Anal. Bound. Elem. 130 (2021) 58–68. https://doi.org/10.1016/j.enganabound.2021.05.009.

[2] C.H. Thai, P.T. Hung, H. Nguyen-Xuan, P. Phung-Van, A size-dependent meshfree approach for magneto-electro-elastic functionally graded nanoplates based on nonlocal strain gradient theory, Eng. Struct. 292 (2023) 116521. https://doi.org/10.1016/j.engstruct.2023.116521.

[3] N.V. Nguyen, H.X. Nguyen, S. Lee, H. Nguyen-Xuan, Geometrically nonlinear polygonal finite element analysis of functionally graded porous plates, Adv. Eng. Softw. 126 (2018) 110–126. https://doi.org/10.1016/j.advengsoft.2018.11.005.

[4] D.-K. Ly, T. Nguyen-Thoi, U. Topal, C. Thongchom, A local–global optimization approach for maximizing the multiphysics frequency response of laminated functionally graded CNTs reinforced magneto-electro-elastic plates, Adv. Eng. Softw. 190 (2024) 103612. https://doi.org/10.1016/j.advengsoft.2024.103612.

[5] C.H. Thai, A.J.M. Ferreira, J. Lee, H. Nguyen-Xuan, An efficient size-dependent computational approach for functionally graded isotropic and sandwich microplates based on modified couple stress theory and moving Kriging-based meshfree method, Int. J. Mech. Sci. 142–143 (2018) 322–338. https://doi.org/10.1016/j.ijmecsci.2018.04.040.

[6] C.H. Thai, V.N.V. Do, H. Nguyen-Xuan, An improved Moving Kriging-based meshfree method for static, dynamic and buckling analyses of functionally graded isotropic and sandwich plates, Eng. Anal. Bound. Elem. 64 (2016) 122–136. https://doi.org/10.1016/j.enganabound.2015.12.003.

[7] T.-V. Vu, Mechanical behavior analysis of functionally graded porous plates resting on elastic foundations using a simple quasi-3D hyperbolic shear deformation theory-based effective meshfree method, Acta Mech. 233 (2022) 2851–2889. https://doi.org/10.1007/s00707-022-03242-2.

[8] T.-V. Vu, H.-L. Cao, Deflection and Natural Frequency Analysis of FG Porous Plates Embedded in Elastic Foundations Using Four-Variable Hyperbolic Quasi-3D Theory, Arab. J. Sci. Eng. 48 (2023) 5407–5445. https://doi.org/10.1007/s13369-022-07423-y.

[9] T.-V. Vu, H.-L. Cao, G.-T. Truong, C.-S. Kim, Buckling analysis of the porous sandwich functionally graded plates resting on Pasternak foundations by Navier solution combined with a new refined quasi-3D hyperbolic shear deformation theory, Mech. Based Des. Struc. 51 (2023) 6227–6253. https://doi.org/10.1080/15397734.2022.2038618.

[10] T.-V. Vu, H.T.T. Nguyen, H. Nguyen-Van, T.-P. Nguyen, J.L. Curiel-Sosa, A refined quasi-3D logarithmic shear deformation theory-based effective meshfree method for analysis of functionally graded plates resting on the elastic foundation, Eng. Anal. Bound. Elem. 131 (2021) 174–193. https://doi.org/10.1016/j.enganabound.2021.06.021.

[11] T.-V. Vu, H. Nguyen-Van, C.H. Nguyen, T.-P. Nguyen, J.L. Curiel-Sosa, Meshfree analysis of functionally graded plates with a novel four-unknown arctangent exponential shear deformation theory, Mech. Based Des. Struc. 51 (2023) 1082–1114. https://doi.org/10.1080/15397734.2020.1863227.

[12] P. Phung-Van, P.T. Hung, H. Nguyen-Xuan, C.H. Thai, Small scale analysis of porosity-dependent functionally graded triply periodic minimal surface nanoplates using nonlocal

strain gradient theory, Appl. Math. Model. 127 (2024) 439–453. https://doi.org/10.1016/j.apm.2023.12.003.
[13] P. Phung-Van, H. Nguyen-Xuan, P.T. Hung, M. Abdel-Wahab, C.H. Thai, Nonlocal strain gradient analysis of honeycomb sandwich nanoscale plates, Thin Wall. Struct. 198 (2024) 111746. https://doi.org/10.1016/j.tws.2024.111746.
[14] P. Phung-Van, P.T. Hung, C.H. Thai, Small-dependent nonlinear analysis of functionally graded triply periodic minimal surface nanoplates, Compos. Struct. 335 (2024) 117986. https://doi.org/10.1016/j.compstruct.2024.117986.
[15] P. Phung-Van, H. Nguyen-Xuan, P.T. Hung, C.H. Thai, Nonlinear isogeometric analysis of magneto-electro-elastic porous nanoplates, Appl. Math. Model. 128 (2024) 331–346. https://doi.org/10.1016/j.apm.2024.01.025.
[16] P. Phung-Van, L.B. Nguyen, P.T. Hung, H. Nguyen-Xuan, C.H. Thai, Nonlocal nonlinear analysis of functionally graded piezoelectric porous nanoplates, Int. J. Mech. Mater. Des. (2024). https://doi.org/10.1007/s10999-023-09701-5.
[17] P.T. Hung, C.H. Thai, P. Phung-Van, Isogeometric free vibration of honeycomb sandwich microplates with the graphene nanoplatelets reinforcement face sheets, Eng. Struct. 305 (2024) 117670. https://doi.org/10.1016/j.engstruct.2024.117670.
[18] P.T. Hung, C.H. Thai, P. Phung-Van, Isogeometric free vibration of functionally graded porous magneto-electro-elastic plate reinforced with graphene platelets resting on an elastic foundation, Comput. Math. Appl. 169 (2024) 68–87. https://doi.org/10.1016/j.camwa.2024.06.005.
[19] Z. Shao, Q. Xia, P. Xiang, H. Zhao, L. Jiang, Stochastic free vibration analysis of FG-CNTRC plates based on a new stochastic computational scheme, Appl. Math. Model. 127 (2024) 119–142. https://doi.org/10.1016/j.apm.2023.11.016.
[20] H. Huo, W. Xu, W. Wang, G. Chen, D. Yang, New non-intrusive stochastic finite element method for plate structures, Comput. Struct. 268 (2022) 106812. https://doi.org/10.1016/j.compstruc.2022.106812.
[21] E. Vanmarcke, M. Shinozuka, S. Nakagiri, G.I. Schueller, Random fields and stochastic finite elements, (n.d.). https://doi.org/10.1016/0167-4730(86)90002-0.
[22] A.D. Kiureghian, J.-B. Ke, The stochastic finite element method in structural reliability, (n.d.).
[23] G. Stefanou, M. Papadrakakis, Assessment of spectral representation and Karhunen–Loève expansion methods for the simulation of Gaussian stochastic fields, Comput. Method. Appl. M. 196 (2007) 2465–2477. https://doi.org/10.1016/j.cma.2007.01.009.
[24] K.K. Phoon, H.W. Huang, S.T. Quek, Comparison between Karhunen–Loeve and wavelet expansions for simulation of Gaussian processes, Comput. Struct. 82 (2004) 985–991. https://doi.org/10.1016/j.compstruc.2004.03.008.
[25] S.P. Huang, S.T. Quek, K.K. Phoon, Convergence study of the truncated Karhunen–Loeve expansion for simulation of stochastic processes, Int. J. Numer. Meth. Eng. 52 (2001) 1029–1043. https://doi.org/10.1002/nme.255.
[26] K.K. Phoon, S.P. Huang, S.T. Quek, Implementation of Karhunen–Loeve expansion for simulation using a wavelet-Galerkin scheme, Probabilist. Eng. Mech. 17 (2002) 293–303. https://doi.org/10.1016/S0266-8920(02)00013-9.
[27] M.-N. Tong, Y.-G. Zhao, Z. Zhao, Simulating strongly non-Gaussian and non-stationary processes using Karhunen–Loève expansion and L-moments-based Hermite polynomial

model, Mech. Syst. Signal Pr. 160 (2021) 107953. https://doi.org/10.1016/j.ymssp.2021.107953.

[28] R.Y. Rubinstein, D.P. Kroese, Simulation and the Monte Carlo method, John Wiley & Sons, 2016.

[29] A. M., A. C.O., An improved response function based stochastic meshless method for problems in elasto-statics, Comput. Method. Appl. M. 372 (2020) 113419. https://doi.org/10.1016/j.cma.2020.113419.

[30] S. Rahman, B.N. Rao, A perturbation method for stochastic meshless analysis in elastostatics, (2001). https://doi.org/10.1002/nme.106.

[31] C.O. Arun, B.N. Rao, S.M. Srinivasan, Stochastic meshfree method for elasto-plastic damage analysis, Comput. Method. Appl. M. 199 (2010) 2590–2606. https://doi.org/10.1016/j.cma.2010.04.009.

[32] S. Rahman, H. Xu, A Meshless Method for Computational Stochastic Mechanics, Int. J. Comput. Meth. En. 6 (2005) 41–58. https://doi.org/10.1080/15502280590888649.

[33] V.G. Kulkarni, Modeling and analysis of stochastic systems, Chapman and Hall/CRC, 2016.

[34] R.G. Ghanem, P.D. Spanos, Stochastic finite elements: a spectral approach, Courier Corporation, 2003.

[35] Z. Shao, X. Li, P. Xiang, A new computational scheme for structural static stochastic analysis based on Karhunen–Loève expansion and modified perturbation stochastic finite element method, Comput. Mech. 71 (2023) 917–933. https://doi.org/10.1007/s00466-022-02259-7.

[36] P.D. Spanos, R. Ghanem, Stochastic finite element expansion for random media, J. Eng. Mech. 115 (1989) 1035–1053. https://doi.org/10.1061/(ASCE)0733-9399(1989)115:5(1035).

[37] M. Grigoriu, Stochastic calculus: applications in science and engineering, Springer Science & Business Media, 2013.

[38] S. Rahman, H. Xu, A univariate dimension-reduction method for multi-dimensional integration in stochastic mechanics, Probabilist. Eng. Mech. 19 (2004) 393–408. https://doi.org/10.1016/j.probengmech.2004.04.003.

[39] X. Liu, P. Xiang, L. Jiang, Z. Lai, T. Zhou, Y. Chen, Stochastic Analysis of Train–Bridge System Using the Karhunen–Loéve Expansion and the Point Estimate Method, Int. J. Str. Stab. Dyn. 20 (2020) 2050025. https://doi.org/10.1142/S021945542050025X.

[40] S. Rahman, Meshfree methods in computational stochastic mechanics, in: Recent Developments in Reliability-Based Civil Engineering, World Scientific, 2006: pp. 187–211. https://doi.org/10.1142/9789812707222_0010.

[41] X. Zhang, B. Chen, Z. Shao, Q. Wang, P. Xiang, A novel stochastic calculation scheme for dynamic response analysis of FG-GPLRC plate subject to a moving load, Acta. Mech. (2023). https://doi.org/10.1007/s00707-023-03813-x.

[42] H. Hong, An efficient point estimate method for probabilistic analysis, Reliab. Eng. Syst. Safe. 59 (1998) 261–267. https://doi.org/10.1016/S0951-8320(97)00071-9.

[43] T. Belytschko, Y.Y. Lu, L. Gu, Element-free Galerkin methods, Int. J. Numer. Meth. Eng. 37 (1994) 229–256. https://doi.org/10.1002/nme.1620370205.

[44] P. Xiang, Q. Xia, L.Z. Jiang, L. Peng, J.W. Yan, X. Liu, Free vibration analysis of FG-CNTRC conical shell panels using the kernel particle Ritz element-free method, Compos. Struct. 255 (2021) 112987. https://doi.org/10.1016/j.compstruct.2020.112987.

[45] C.H. Thai, T.D. Tran, P. Phung-Van, A size-dependent moving Kriging meshfree model for

deformation and free vibration analysis of functionally graded carbon nanotube-reinforced composite nanoplates, Eng. Anal. Bound. Elem. 115 (2020) 52–63. https://doi.org/10.1016/j.enganabound.2020.02.008.

[46] Z. Shao, H. Zhao, P. Zhang, X. Xie, A.S. Ademiloye, P. Xiang, A meshless computational framework for a modified dynamic system of vehicle coupled with plate structure, Eng. Struct. 312 (2024) 118140. https://doi.org/10.1016/j.engstruct.2024.118140.

[47] Q. Xia, P. Xiang, L. Peng, H. Wang, L. Jiang, Interlayer shearing and bending performances of ballastless track plates based on high-order shear deformation theory (HSDT) for laminated structures, Mech. Adv. Mater. Struc. (2023) 1–25. https://doi.org/10.1080/15376494.2022.2139441.

[48] Q. Xia, P. Xiang, L. Jiang, J. Yan, L. Peng, Bending and free vibration and analysis of laminated plates on Winkler foundations based on meshless layerwise theory, Mech. Adv. Mater. Struc. 29 (2022) 6168–6187. https://doi.org/10.1080/15376494.2021.1972497.

[49] S. Kwak, H. Kim, K. Kim, Dynamic Analysis of Laminated Composite Wave Plate in Thermal Environment Using Meshfree Method, J. Vib. Eng. Technol. 12 (2024) 1153–1176. https://doi.org/10.1007/s42417-023-00899-4.

[50] C.H. Thai, A.J.M. Ferreira, H. Nguyen-Xuan, Naturally stabilized nodal integration meshfree formulations for analysis of laminated composite and sandwich plates, Compos. Struct. 178 (2017) 260–276. https://doi.org/10.1016/j.compstruct.2017.06.049.

[51] C.H. Thai, A.J.M. Ferreira, T. Rabczuk, H. Nguyen-Xuan, A naturally stabilized nodal integration meshfree formulation for carbon nanotube-reinforced composite plate analysis, Eng. Anal. Bound. Elem. 92 (2018) 136–155. https://doi.org/10.1016/j.enganabound.2017.10.018.

[52] A.-A. Daikh, M.-O. Belarbi, D. Ahmed, M.S.A. Houari, M. Avcar, A. Tounsi, M.A. Eltaher, Static analysis of functionally graded plate structures resting on variable elastic foundation under various boundary conditions, Acta. Mech 234 (2023) 775–806. https://doi.org/10.1007/s00707-022-03405-1.

[53] A.A. Daikh, M.S.A. Houari, M.A. Eltaher, A novel nonlocal strain gradient Quasi-3D bending analysis of sigmoid functionally graded sandwich nanoplates, Compos. Struct. 262 (2021) 113347. https://doi.org/10.1016/j.compstruct.2020.113347.

[54] C.H. Thai, A.J.M. Ferreira, H. Nguyen-Xuan, P. Phung-Van, A size dependent meshfree model for functionally graded plates based on the nonlocal strain gradient theory, Compos. Struct. 272 (2021) 114169. https://doi.org/10.1016/j.compstruct.2021.114169.

[55] J.N. Reddy, A simple higher-order theory for laminated composite plates, (1984). https://doi.org/10.1115/1.3167719.

[56] G.R. Liu, Y.T. Gu, A matrix triangularization algorithm for the polynomial point interpolation method, Comput. Method. Appl. M. 192 (2003) 2269–2295. https://doi.org/10.1016/S0045-7825(03)00266-4.

[57] Z. Shao, P. Xiang, H. Zhao, P. Zhang, X. Xie, L. Gan, W. Li, B. Yin, K.M. Liew, A novel train–bridge interaction computational framework based on a meshless box girder model, Adv. Eng. Softw. 192 (2024) 103628. https://doi.org/10.1016/j.advengsoft.2024.103628.

[58] J.-S. Chen, C.-T. Wu, S. Yoon, Y. You, A stabilized conforming nodal integration for Galerkin mesh-free methods, Int. J. Numer. Meth. Engng. 50 (2001) 435–466. https://doi.org/10.1002/1097-0207(20010120)50:2<435::AID-NME32>3.0.CO;2-A.

[59] C.H. Thai, A.J.M. Ferreira, M.A. Wahab, H. Nguyen-Xuan, A moving Kriging meshfree method with naturally stabilized nodal integration for analysis of functionally graded material sandwich plates, Acta Mech. 229 (2018) 2997–3023. https://doi.org/10.1007/s00707-018-2156-9.
[60] C.H. Thai, P. Phung-Van, A meshfree approach using naturally stabilized nodal integration for multilayer FG GPLRC complicated plate structures, Eng. Anal. Bound. Elem. 117 (2020) 346–358. https://doi.org/10.1016/j.enganabound.2020.04.001.
[61] B. Sudret, A. Der Kiureghian, Stochastic finite element methods and reliability: a state-of-the-art report, Department of Civil and Environmental Engineering, University of California …, 2000.
[62] G.-R. Liu, Meshfree methods: moving beyond the finite element method, CRC press, 2009.
[63] A.M. Zenkour, Bending analysis of functionally graded sandwich plates using a simple four-unknown shear and normal deformations theory, J. Sandw. Struct. Mater. 15 (2013) 629–656. https://doi.org/10.1177/1099636213498886.
[64] S.S. Tomar, M. Talha, Influence of material uncertainties on vibration and bending behaviour of skewed sandwich FGM plates, Compos. Part. B-Eng. 163 (2019) 779–793. https://doi.org/10.1016/j.compositesb.2019.01.035.
[65] J. Yang, K.M. Liew, S. Kitipornchai, Stochastic analysis of compositionally graded plates with system randomness under static loading, Int. J. Mech. Sci. 47 (2005) 1519–1541. https://doi.org/10.1016/j.ijmecsci.2005.06.006.